

# The three-dimensional shear velocity structure of the mantle from the inversion of body, surface and higher-mode waveforms

Charles Mégnin\* and Barbara Romanowicz

U. C. Berkeley Seismological Laboratory, Berkeley, CA 94720, USA. E-mail: pepe@seismo.berkeley.edu

Accepted 2000 June 13. Received 2000 May 10; in original form 1999 September 3

## SUMMARY

We present a 3-D model of shear heterogeneity ( $V_{sh}$ ) in the whole mantle, derived from the inversion of hand-picked body, surface and higher-mode waveforms. The forward and inverse problems are formulated using the non-linear asymptotic coupling theory, the zeroth-order asymptotic expansion of a Born seismogram computed by normal mode summation and including coupling across mode branches. We invert iteratively for mantle heterogeneity and for centroid moment tensors until convergence. Our model, SAW24B16, is parametrized laterally in spherical harmonics up to degree 24 and radially in 16 cubic b-splines with knots spaced to reflect the data sampling with depth.

The power spectrum of the model is dominated by heterogeneity in the boundary layers at low degrees: degrees 5 and 6 near the surface and degree 2 near the core–mantle boundary. The rest of the lower mantle is dominated by degree 3. We find significant heterogeneity up to spherical harmonic degree 24 in the transition zone and the uppermost part of the lower mantle.

Our model displays three slow domains extending continuously between uppermost and lowermost mantle, one originating under Africa and two in the Pacific. The results of our modelling also suggest an interaction near the surface between the anomalies in the Pacific and the network of mid-ocean ridges in the East Pacific, and between the African anomaly and the low-velocity zone in the Red Sea, the East African Rift, the Mid-Indian Ridge and the Mid-Atlantic Ridge. These anomalies appear to ascend into the upper mantle without altering their shape near the 670 km discontinuity.

Fast anomalies accumulate near the 670 km discontinuity under the Southern Kurile, the Japan trench and the Izu arc, with little or no penetration into the lower mantle, in agreement with results from a variety of regional studies. Cross-sections through subduction zones such as the Marianas, Tonga–Kermadec, Java, the palaeosubduction zone beneath North America and the Peru–Chile trench show continuous fast structures penetrating into the lower mantle, with the depth of penetration varying from region to region.

The distribution of both fast and slow anomalies near 670 km thus suggests that the discontinuity does not act as a strong barrier to upgoing and downgoing flow between the upper and the lower mantle.

**Key words:** inversion, mantle, mode coupling, seismic structure, tomography, waveform analysis.

## 1 INTRODUCTION

Following pioneering work in the upper mantle (Woodhouse & Dziewonski 1984; Nataf *et al.* 1986) and in the lower mantle (Dziewonski *et al.* 1977), 3-D models of the whole mantle have been derived by research groups using different modelling tech-

niques and a variety of data sets: among recent studies, Grand (1994) and Grand *et al.* (1997) computed traveltimes from body waveforms, (Masters *et al.* 1996) combined absolute and differential traveltimes with phase velocity measurements of surface waves and normal mode data, van der Hilst *et al.* (1997) used ISC *P* and *pP* traveltimes residuals with source parameters relocated by Engdahl *et al.* (1998) to derive a compressional velocity model, Vasco *et al.* (1994) used *P* and *S* ISC data

\* Author to whom correspondence should be addressed.

to constrain compressional and shear velocity structure in the mantle, Su *et al.* (1994) and Liu & Dziewonski (1994, 1998) combined absolute and differential traveltimes measurements with surface and body waveform data modelled with a surface wave formalism, and Li & Romanowicz (1996) derived a model exclusively from hand-picked *SH* waveforms by formulating the forward and inverse problems in a theoretical normal mode framework valid for both body and surface waves.

Although there is a general consensus regarding the long-wavelength components of these models, disagreements remain in the details. In addition to differences in data sets, one of the sources of the discrepancies is the accuracy of the theoretical formalism used and another is the parametrization. The use of waveform data allows us to depart from the infinite-frequency, ray-optic approximation that constitutes the theoretical foundation of 3-D seismic velocity models computed from traveltimes data such as those of Vasco & Johnson (1998), van der Hilst *et al.* (1997), Liu & Dziewonski (1994) and Su *et al.* (1994). In addition to providing a more accurate approach to the modelling of seismic data in general, waveform tomography can make use of phases diffracted on the core–mantle boundary (CMB) that cannot be treated with the ray-optic approximation. The waveform approach also makes use of all of the information contained in the seismic signal, in particular of energy corresponding to the simultaneous arrival of different phases (e.g. *SS* and *ScS* at an epicentral distance of  $45^\circ$ ), and therefore improves the sampling at depth in comparison with traveltimes studies, which are restricted to using well-isolated phases on the seismogram.

The quality of tomographic images is not only related to the accuracy of the theoretical formalism, but can be improved by a judicious choice of parametrization. For example, Bijwaard *et al.* (1998) have attempted to achieve uniform resolution by locally varying the cell size of their model to minimize the difference in ‘hit count’ among cells. Such refinements are of course precluded by the use of global basis functions, and tomographers are increasingly abandoning their use in favour of functions with local support. In particular, several recent global models have been derived using cubic b-splines in the radial direction. Masters *et al.* (1996) and Su & Dziewonski (1996) used evenly spaced splines in their modelling, and Liu & Dziewonski (1998) modified this approach and distributed the spline knots of their models S16U6L8 and S16VB14 to reflect the data sampling at depth. Using the method derived by Wang & Dahlen (1995), Wang *et al.* (1998) derived global phase velocity maps using expansions in spherical splines in the lateral direction, and allowed the grid size to be smaller in regions of high coverage.

On the other hand, Li & Romanowicz (1996) derived a degree 12 model of *SH* shear wave velocity parametrized radially in Legendre polynomials, constructed using waveforms of surface and body waves, modelled with the ‘non-linear asymptotic coupling theory’ (NACT) formalism of Li & Romanowicz (1995). We use their methodology to derive a higher-degree model, adding overtone surface waveforms of the first and second orbits to the existing data set, as well as more recent body wave and fundamental-mode surface wave data. Our data set consists exclusively of hand-picked waveforms, with all phase types fitted with the same theoretical formalism. The present model is parametrized radially in cubic b-splines with knots spaced to reflect the distribution of rays at depth, a first step towards a fully locally parametrized whole-mantle model.

## 2 MODEL CHARACTERISTICS

### 2.1 Data

We consider a collection of hand-picked time-domain transverse-component waveforms for 738 events recorded during the period 1977–1997 at 200 IRIS and GEOSCOPE network stations (Fig. 1). Our data set consists of body waves, and first- and second-orbit fundamental and overtone surface wave trains (see Table 1). The corresponding body wave phases are listed in Table 2.

Higher-mode waveforms provide coverage in the upper 1972). They have been modelled for this purpose in recent studies (Stutzmann & Montagner 1994; van Heijst & Woodhouse 1999) using techniques aimed at resolving the dispersion characteristics of each individual overtone (Stutzmann & Montagner 1993; van Heijst & Woodhouse 1997). Complete time-domain waveforms have also been used (e.g. Woodhouse & Dziewonski 1984; Tanimoto 1989; Su *et al.* 1994), but in these approaches, fundamental and overtone information of all orbits is extracted simultaneously. In the present study, overtone data are also modelled in the time domain, but whenever possible, we fit each orbit separately and independently from the fundamental surface waves. The advantage of this procedure is described below.

In Fig. 2, we show an example of body waveforms for a  $M_w = 7.1$  1996 Kurile Islands event recorded at station DRV in Antarctica. We compare the data low-pass filtered at 32 s (middle trace) with a synthetic seismogram computed in the spherically symmetric model PREM (Dziewonski & Anderson 1981), corrected for ellipticity effects (bottom trace) and filtered in the same fashion. The same record is plotted with a 16 s

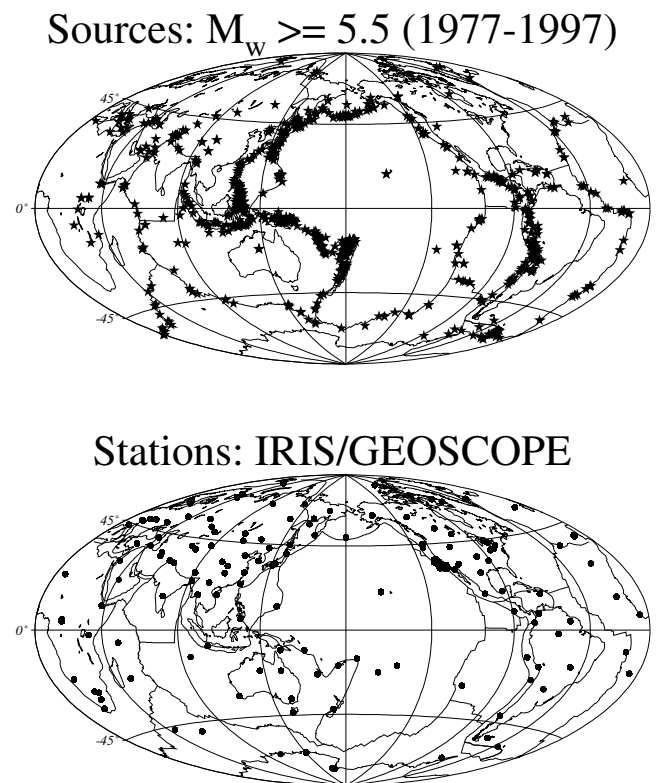


**Figure 1.** Top: distribution of events used in this study. Bottom: distribution of IRIS and GEOSCOPE station locations.

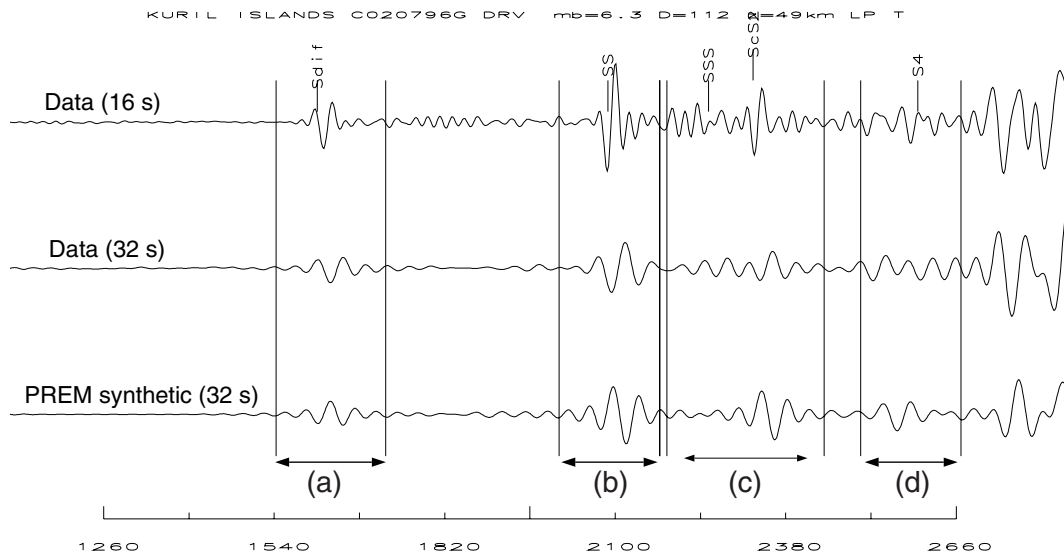


**Figure 2.** Example of data selection procedure for a February 1996  $M_w = 7.1$  event in the Kurile recorded at station DRV, Antarctica ( $\Delta = 112^\circ$ ). Top trace: 16 s deconvolved data; middle trace: 32 s deconvolved data; bottom trace: 32 s PREM synthetic. Each body wavepacket is hand-selected individually (a)  $S$  diffracted, (b)  $SS$ , (c)  $S_3$  and  $ScS_2$ , and (d)  $S_4$ .

**Table 1.** Summary of the data used in this study. The frequency band is expressed in seconds and corresponds to the high cut-off, high corner, low corner and low cut-off periods respectively. A cosine taper is applied between the corner and cut-off frequencies. Residual variances with respect to model SAW24B16 are given in the third column.

Data type	Number of traces	Period band (s)	Residual variance
Body waveforms	11 286	300, 180, 37, 31.4	0.532
Surface waveforms	9360	400.2, 250.3, 100.1, 80	0.404
Higher-mode waveforms	1440	400.2, 250.3, 100.1, 80	0.563

low-pass filter to facilitate phase identification and selection (top trace). Each relevant energy wavepacket in the seismic trace is picked individually. In this particular instance, the phases  $S_{\text{diff}}$ ,  $SS$ ,  $SSS$  &  $ScS_2$  and  $S_4$  were selected. We have shown in a recent publication that isolating the different energy wavepackets in a seismogram increases resolution at depth, and in particular that fitting the  $S_{\text{diff}}$  independently from the

rest of the seismic trace considerably improves resolution in the lowermost mantle (Méglin & Romanowicz 1999). We adopt the same approach with the surface waveforms and separate the fundamental modes from the overtones whenever possible, as amplitudes on long-period seismograms are generally dominated by fundamental-mode energy. Similarly, we separate the first-orbit arrivals from the second orbit. This is particularly useful at short epicentral distances where the arrivals corresponding to minor arc travel paths display stronger amplitudes than those of the major arc. Another important advantage of using waveforms in tomography is that it allows one to accommodate phases arriving simultaneously, but sampling different parts of the mantle. This increases the resolution in comparison with the traveltimes approach, which requires well-isolated phase arrivals.

While events are evenly distributed between the Northern and Southern Hemispheres, three out of four seismic stations are located in the Northern Hemisphere (Fig. 1). We thus expect images to be better resolved in the north than in the south, in particular in the lowermost mantle, which is sampled only by body waves. In the upper mantle and the upper part of the lower mantle, the major arc fundamental and overtone surface waveform travel paths make up to some extent for the scarcity of stations in the Southern Hemisphere.

**Table 2.** Number of body wave phases used in this study.

Body phase	Number of occurrences
$S$ and $sS$	5865
$SS$ and $sSS$	7277
$S_3$ and $sS_3$	5003
$S_4$ and $sS_4$	2713
$ScS$ and $sScS$	4671
$ScS_2$ and $sScS_2$	3423
$ScS_3$ and $sScS_3$	184
$S_{\text{diff}}$ and $sS_{\text{diff}}$	1220
Unidentified phases	941
Total	31 084

As the distribution of data in the 3-D earth is irregular, we use a weighting scheme to prevent images of the whole mantle from being controlled by the regions sampled by the most abundant travel paths. For each wavepacket, we compute a measure of redundancy with respect to all the other wavepackets in the data set. We then assign to the wavepacket a weight inversely proportional to the square root of the redundancy estimate. This procedure is detailed in Li & Romanowicz (1996), Appendix A.

## 2.2 Theory

The waveforms are modelled using NACT, developed by Li & Romanowicz (1995). The NACT formalism uses the Born approximation (e.g. Woodhouse 1983; Tanimoto 1984), with the coupling of the modes taken into account both along and across mode branches. It has been shown that across-branch coupling is necessary to model body waveforms (e.g. Li & Tanimoto 1993; Marquering & Snieder 1995). With NACT, the mode coupling is computed asymptotically to order zero, which restricts the sensitivity of the synthetic waveforms to the structure along the great-circle path (Romanowicz 1987; Park 1987). Such a seismogram is expressed as a sum on modes

$k$  and  $k'$ , the eigenvibrations of the PREM earth:

$$u(t) = \sum_k \left[ A_k \exp(i\tilde{\omega}_k t) (1 - it\delta\omega_k) + \sum_{qh} \left( a_h^q \sum_{k'} A_{kk'}^q + b_h^q \sum_{k'} B_{kk'}^q \right) \right], \quad (1)$$

where  $\tilde{\omega}_k = \omega_k + \delta\omega_k$ , and  $\delta\omega_k$  is the ‘minor arc average term’, which corresponds to along-branch coupling (e.g. Romanowicz 1987), and the coefficients  $a_h^q$  and  $b_h^q$  characterize the model in the great-circle coordinates along the source–receiver path, which is decomposed in  $q$  radial functions and in a Fourier series sum on  $h$ . We refer the reader to Li & Romanowicz (1995) for a detailed description of each term. The point we wish to make here is that the seismogram is non-linearly related to the earth’s structure (eq. 2) through  $\delta\omega_k$ , and linearly through the across-branch coupling terms  $A_{kk'}^q$  and  $B_{kk'}^q$ .

## 2.3 Parametrization

The shear velocity model we construct, SAW24B16, is expressed as a perturbation  $\delta v_{\text{sh}}(r, \theta, \phi)/v_{\text{sh}}^{\text{PREM}}(r)$  from the spherically symmetric model PREM (Dziewonski & Anderson 1981), and is

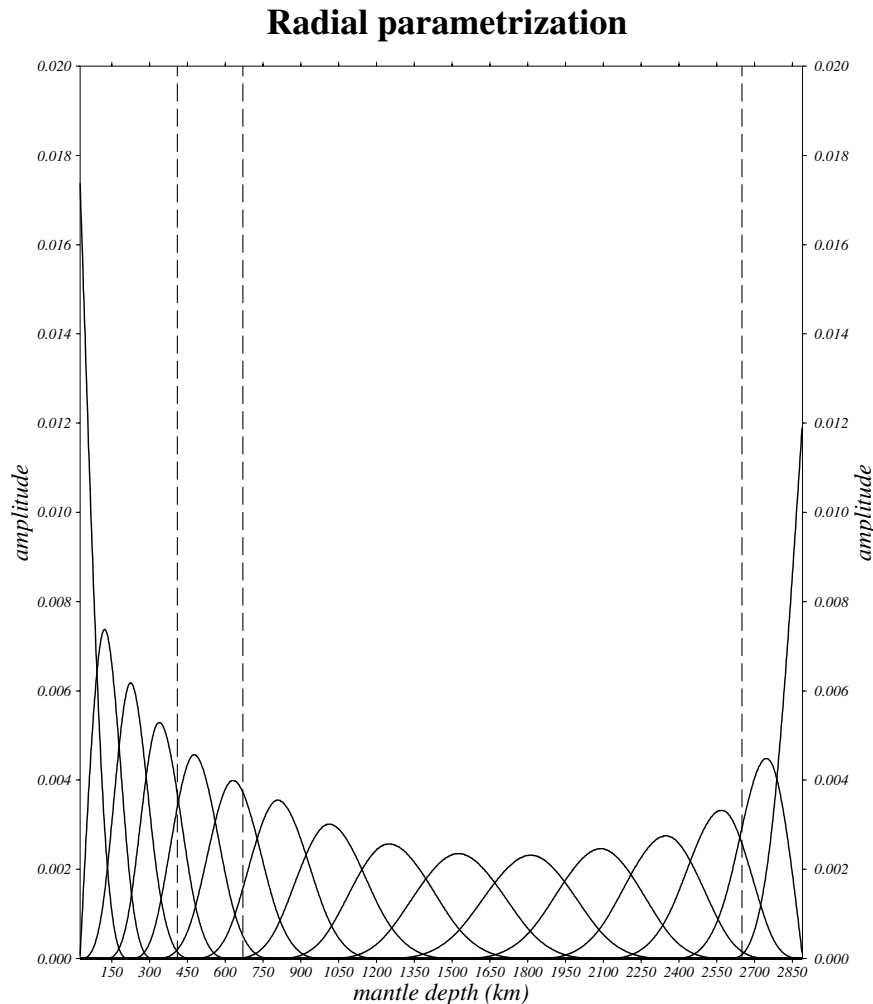


**Figure 3.** Distribution of the 16 cubic b-splines used to parametrize the model radially, as a function of mantle depth. Each spline is normalized to unit area.

parametrized laterally in spherical harmonics up to degree 24, and radially in 16 cubic b-splines, continuously distributed with 6 knots in the upper mantle and 10 in the lower mantle:

$$\frac{\delta v_{\text{sh}}(r, \theta, \phi)}{v_{\text{sh}}^{\text{prem}}(r)} = \sum_{k=0}^{15} \sum_{s=0}^{24} \sum_{t=-s}^s k a_s^t B_k(r) Y_s^t(\theta, \phi), \quad (2)$$

where  $B_k(r)$  are cubic b-splines, defined in Appendix A, and  $Y_s^t(\theta, \phi)$  are fully normalized spherical harmonics as defined in Edmonds (1960). The lateral resolution is about 850 km at the surface and 450 km in the lowermost mantle. The spline knots are spaced to reflect the radial resolution, varying smoothly from 100 km near the surface to 300 km in the mid-mantle and 150 km in the lowermost mantle. Their distribution with depth and their amplitude are shown in Fig. 3. To avoid possible artefacts in transition zone images, we opted for a continuous parametrization across the 670 km discontinuity. Splitting the parametrization between upper and lower mantle presents the advantage of accommodating the difference in resolution between the shallow and the deep parts of the mantle. However, it also introduces some level of decoupling as observed, for example, in the radial correlation functions, and may impact on our analysis of continuity of structure across the 670 km discontinuity. Allowing the knot spacing to vary accommodates variability in radial resolution and does not bias transition zone images.

## 2.4 Inversion

The inverse problem is solved using a stochastic formalism (e.g. Jackson 1979; Tarantola & Valette 1982), and the finite-dimensional model is obtained by the recursive application of a Newton scheme to the Fréchet derivatives of the  $\ell^2$ -norm objective function. A detailed description of the inversion procedure is given in Li & Romanowicz (1996).

SAW24B16 is derived by inverting iteratively for 3-D velocity perturbations in the mantle, and for Moho depth, and for perturbations to source parameters from those of the Harvard centroid moment tensor (CMT) catalogue (moment tensor, hypocentre location and origin time). Attenuation in the mantle is taken into account by using the radial quality factor model QL6 (Durek & Ekström 1996), which we hold fixed throughout all the inversion steps. We introduce the contribution to the waveforms from undulations of the topography and bathymetry using the model ETOPO-5 (1990) and construct an *a priori* model of Moho depth representing the difference between the continental and oceanic regions, as in Woodhouse & Dziewonski (1984). Higher-frequency data are needed to constrain variations in Moho depth, and in this study we inverted for Moho topography only for the purpose of reducing the error resulting from contributions from 3-D crustal variations, which are neglected here. The 3-D model derived proved to be independent of the damping applied to Moho perturbations, suggesting that this step does not bias the results.

In the inversion of the data, we use the set of damping parameters constructed to recover the 3-D spherical convection model GEMLAB 1 (Bunge *et al.* 1998) in a synthetic test. This model incorporates the effects of many parameters relevant to Earth's dynamics, in particular two phase transitions, 20 per cent partial bottom heating, viscosity layering between the upper and the lower mantle, and the history of plate motions since the mid-Mesozoic. Using a simulated annealing algorithm (Press *et al.* 1994), we computed the set of *a priori* constraints

that minimize the  $\ell^2$  norm of the difference between the input model scaled to velocity perturbations and the inversion of a noise-free synthetic data set. Details of this procedure are given in Mégnin & Romanowicz (2000).

We conducted three rounds of inversion. Starting from the degree 12 model of Li & Romanowicz (1996), we inverted for 3-D mantle heterogeneity using as initial moment tensors the results from Li & Romanowicz (1996) for the data prior to 1996, and from the CMT catalogue for the more recent data. Holding the obtained 3-D model fixed, we then performed an inversion for a new set of source parameters, inverting simultaneously for the CMTs, origin time and source location. Holding in turn the new set of sources fixed, we re-inverted for 3-D mantle heterogeneity. For each round of inversion, several iterations (typically three) are performed until convergence. The improvement of the fit to the data resulting from the CMT inversions exceeds 10 per cent. The residual variance of the final model with respect to each phase type is given in Table 1.

## 3 RESULTS

### 3.1 Overview

#### 3.1.1 Surface wave coverage

In Fig. 4 (top), we show the coverage corresponding to our fundamental surface wave collection. This is expressed as the logarithm of the number of  $1^\circ$  great-circle segments in each

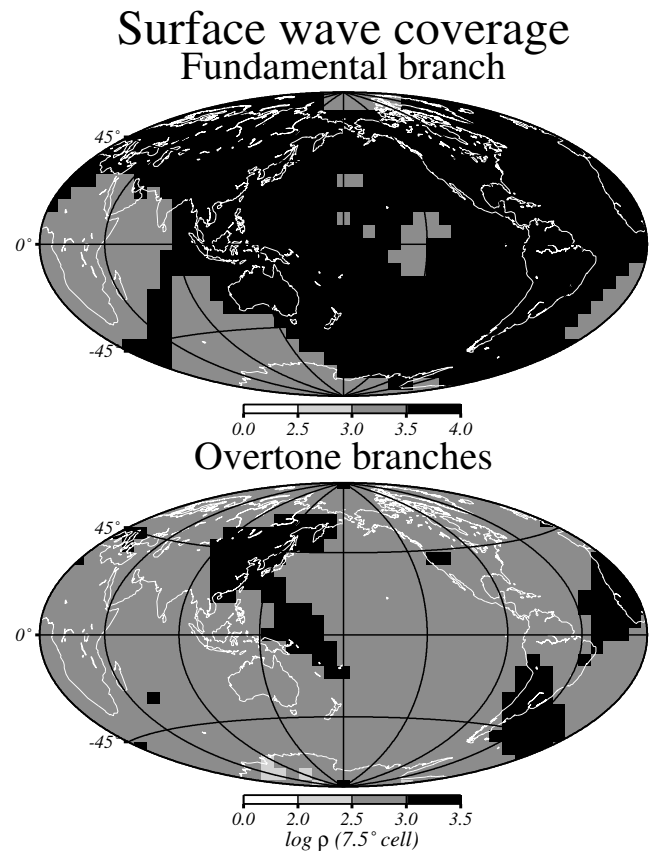


**Figure 4.** Top: Love wave density coverage, expressed as the logarithm of the number of  $1^\circ$  segments in each  $7.5^\circ \times 7.5^\circ$  cell ( $\rho$ ). Bottom: same as top figure for the higher-mode phases. Note the difference in scale between the two figures.

$7.5^\circ \times 7.5^\circ$  cell (the wavelength corresponding to degree 24), corrected for latitude. The density coverage corresponding to the region sampled by surface waves is everywhere between 1000 and 10 000 hit counts per cell. At the bottom of the figure, we show the same measure for the higher-mode arrivals. The coverage density exceeds 100 hit counts per cell everywhere and 1000 hit counts per cell in the West Pacific region. The collection of the overtone branches in this data set therefore provides ample constraints to image the transition zone and the uppermost part of the lower mantle at all latitudes, and in particular the West Pacific slab.

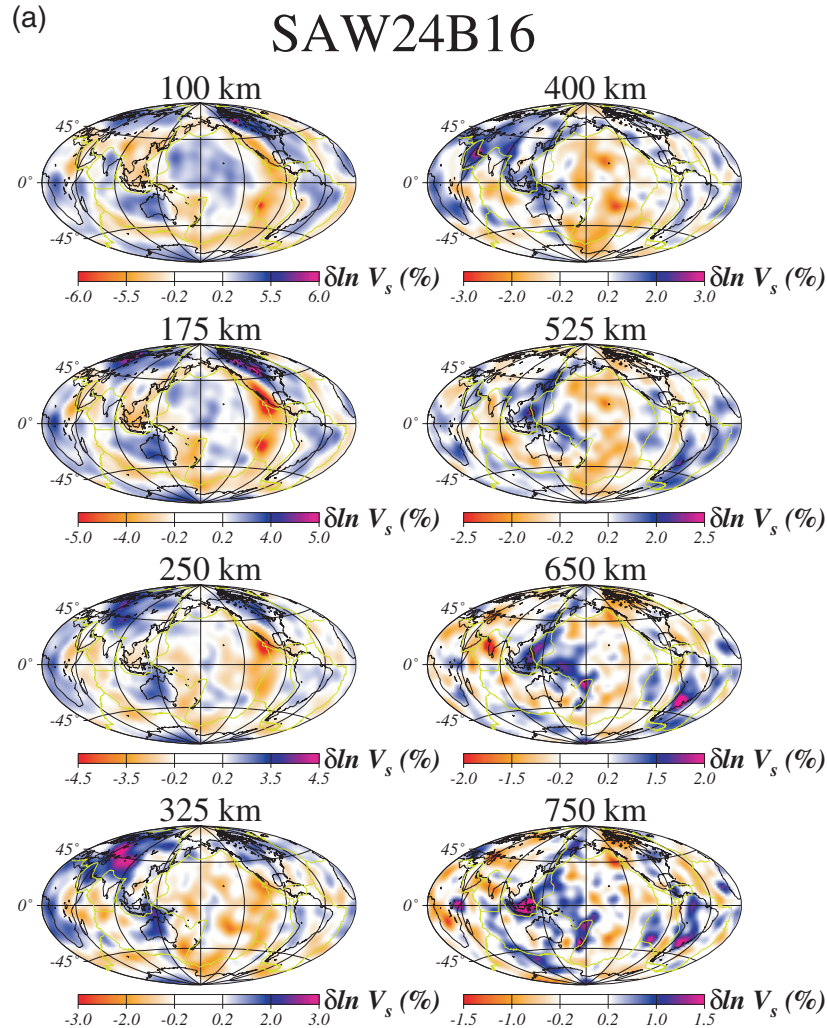
### 3.1.2 Depth sections

Fig. 5(a) shows lateral cross-sections of the model at mantle depths between 100 and 750 km. The largest amplitudes are at the shallowest depths. As expected, the shallower sections display fast velocity anomalies under continents. At 100 km the peak anomaly in the East Pacific Rise is  $-6.3$  per cent and it is  $+6.2$  per cent in the North American Craton. We find, in agreement with van der Lee & Nolet (1997), strong low-velocity anomalies below the Western United States ( $-6.3$  per cent at

100 km), extending to 300 km depth. Slow domains are observed in the model below the mid-ocean ridges in the East Pacific, mid-Atlantic and in the Indian ocean. The back-arc basins of the West Pacific are also associated with slow anomalies, which dominate the image in this region of the uppermost mantle and therefore conceal the onset of subduction.

Significant variations in the depth extent of the fast anomalies below the cratons is observed. Bearing in mind that the radial resolution is of the order of 100 to 150 km at upper mantle depths, the fast anomaly beneath the Brazilian shield disappears below about 250 km, but it extends down to 400 km under North America, Eurasia and Australia. Fast velocities are observed down to 500 km beneath Africa and are the deepest such feature in the model. The heterogeneity field at 650 km is largely dominated by fast velocities corresponding to subduction in the West Pacific and the South American continent, an observation still valid at 750 km.

The persistent signature of subduction is the most noticeable feature in the upper part of the lower mantle (Fig. 5b, 850 km). Fast velocity anomalies with amplitudes above 1 per cent are observed at 850 km beneath Tonga–Kermadec, Java and the Marianas. They disappear beneath Japan and the Southern



**Figure 5.** (a) Horizontal cross-sections of model SAW24B16 at depths between 100 and 750 km. (b) Horizontal cross-sections of model SAW24B16 at representative lower mantle depths.

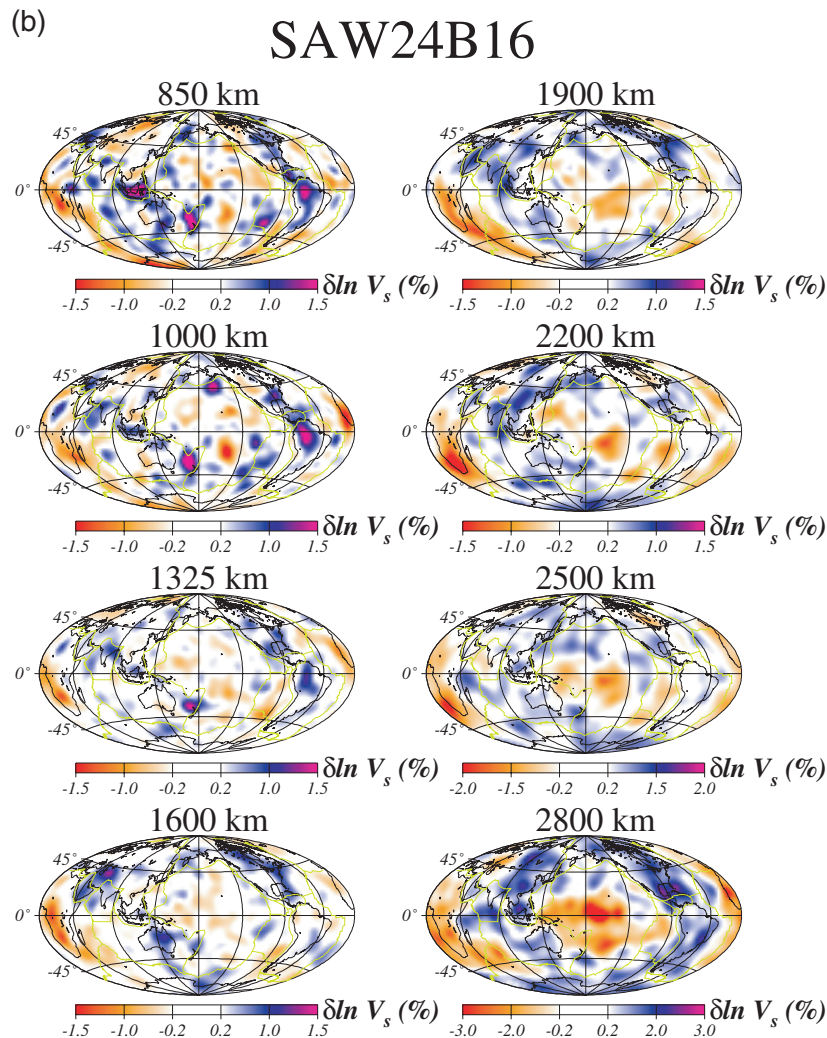


Figure 5. (Continued.)

Kuriles but are strong in the Kamchatka region, in agreement with Ding & Grand (1994). Fast velocities are also present under South America, and the fast anomaly associated with the Farallon palaeosubduction is seen to migrate eastwards with depth (Grand 1994; Grand *et al.* 1997; van der Hilst *et al.* 1997).

At 1600 km, the fast anomaly associated with subduction under South America has largely disappeared. In contrast, the Farallon plate continues its eastward progression with depth, and is prominent below the northwestern part of the Atlantic Ocean. Both these features are in agreement with the model of Grand (1994).

A large-scale slow anomaly is observed under Africa, throughout the entire depth range of the lower mantle, becoming more focused around 2000 km. Another slow domain under the Central Pacific, also present throughout the lower mantle, shows stronger amplitudes at depths greater than 2000 km as well. In the lowermost mantle (2800 km), the distribution of heterogeneity is dominated by a degree 2 pattern, consisting of two slow domains, one under Africa, one in the mid-Pacific, surrounded by a fast anomaly in the circum-Pacific (see Fig. 5b at 2800 km and Fig. 6). This agrees with many other tomographic results (e.g. for the most recent models, Resovsky & Ritzwoller 1999; Grand *et al.* 1997; Li & Romanowicz 1996;

Masters *et al.* 1996; Liu & Dziewonski 1994). Peak amplitudes in the lowermost mantle are  $-3.5$  per cent under the mid-Pacific and  $+2.5$  per cent under the Gulf of Mexico.

### 3.1.3 Spectrum

In Fig. 6 (left), we show the spectral decomposition of SAW24B16. Model amplitudes are shown as a function of wavelength (horizontal axis) and mantle depth (vertical axis). The image is dominated by the top and bottom boundary layers: the tectonic signature at degrees 5 and 6 in the uppermost mantle, and a strong degree 2 component in D''. To enhance the picture in the mid-mantle, the spectral heterogeneity map is normalized in Fig. 6 (centre) by the rms amplitude at each depth (Fig. 6, right). Each mantle depth has a unique dominant wavelength: degree 5 in the uppermost mantle, degree 1 above the transition zone, degree 2 in the transition zone. The lower mantle is dominated by spectral peaks at degrees 0, 3 and 2, and D'' by degree 2. The character of the model in the depth range between 60 and 900 km is 'white', with significant heterogeneity up to degree 24.

In Fig. 7, we compare the rms amplitudes of SAW24B16 with that of two recent  $V_s$  models. The radial profile of our

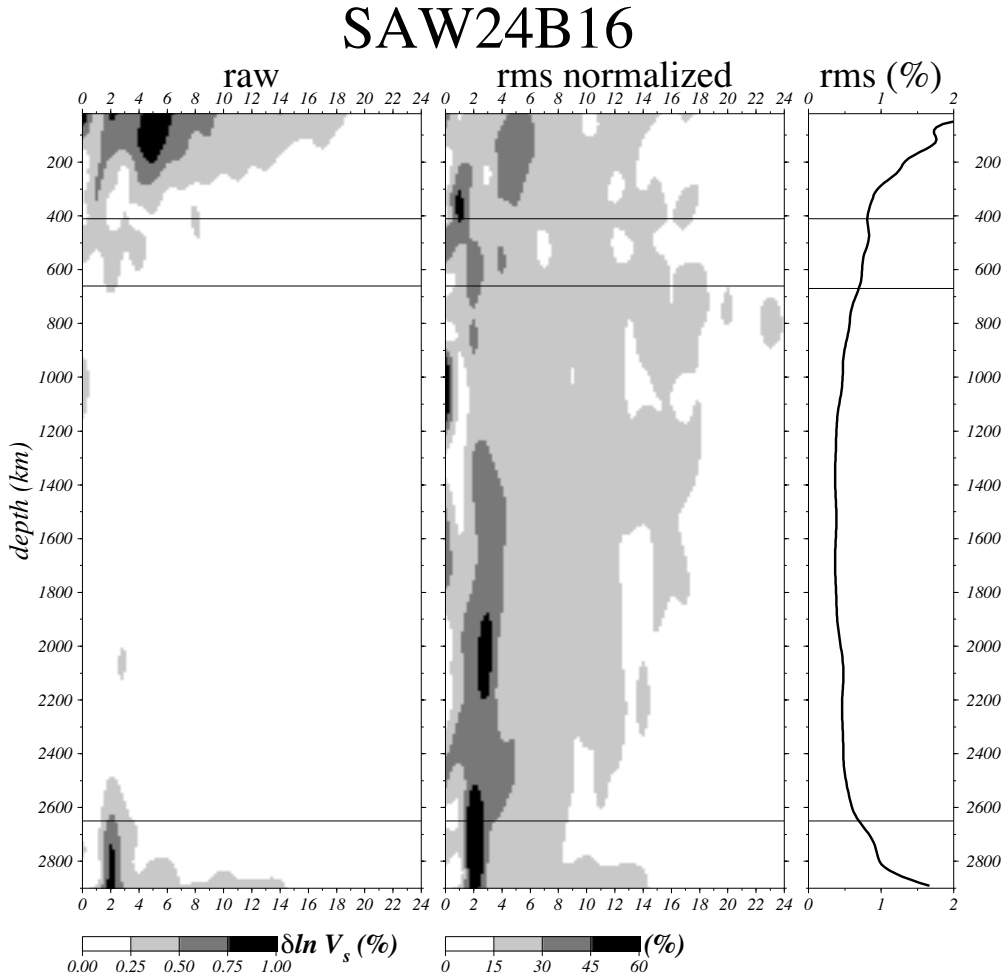


**Figure 6.** Spectral heterogeneity maps representing rms as a function of depth and the degree in the spherical harmonic expansion of model SAW24B16. Left: absolute spectrum; centre: same as left map but normalized by the rms at each depth; right: rms amplitudes as a function of depth, all degrees included.

model (solid line) is close to that of Gu & Dziewonski (2000) (dashed line), but amplitudes in the mid-mantle are significantly higher than those of Grand (1994) (dotted line).

### 3.1.4 Lowermost mantle coverage

In Fig. 8 (top), we show the lowermost mantle coverage, represented by the projection on the CMB of the  $S_{\text{diff}}$  and  $sS_{\text{diff}}$  phases (horizontal lines) and the  $ScS$ ,  $sScS$  and  $ScS$  and  $sScS$  multiples (dots). The disproportionate sampling between the Northern and Southern Hemispheres is directly related to the receiver distribution (see Fig. 1). The coverage density for the reflected phases (middle left) and the diffracted phases (middle right) is expressed as  $\log(1+n)$  at the CMB (as in Fig. 4), where  $n$  is, for the diffracted phases, the number of  $1^\circ$  length ray path segments in each  $7.5^\circ \times 7.5^\circ$  degree cell corrected for latitude, and, for the reflected phases, the number of hit counts at the bounce points on the CMB. It is interesting to note that a level of complementarity exists between the two data sets, the most prominent being under Australia (well sampled by the  $ScS$  but not by the  $S_{\text{diff}}$ ) and the Southeast Pacific along  $225^\circ$  longitude (sampled by the  $S_{\text{diff}}$  but not by the  $ScS$ ). At the bottom of the figure we show the total coverage at the bottom of the mantle, resulting from the combination of all CMB-reflected and

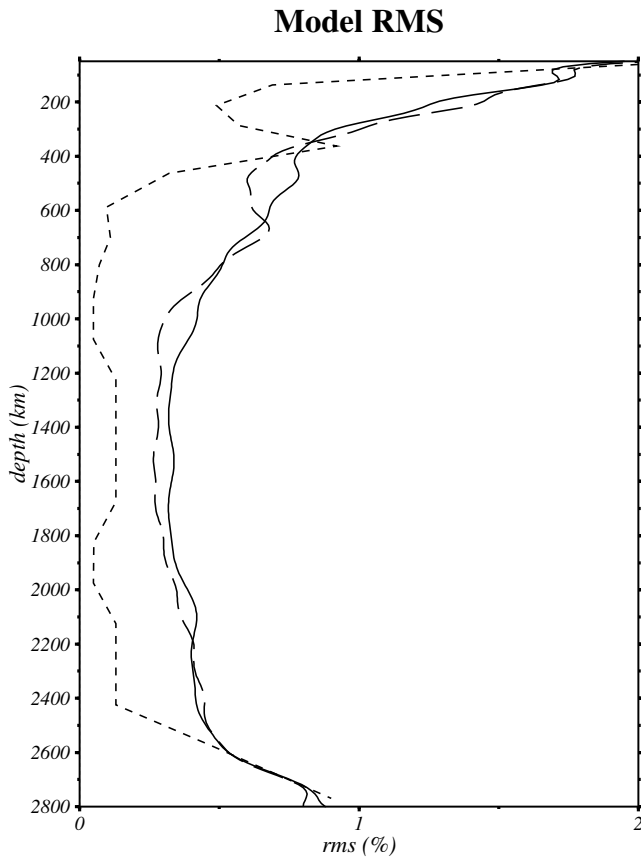
diffracted phases. The sampling is best below the North Pacific, the mid-Pacific and Asia and poorest in the South Atlantic and south of Australia.

### 3.2 Subduction under the Americas

Fig. 9(a) (top) shows a horizontal cross-section of the western part of the North and South American continents at 175 km depth, centred on the East Pacific Rise. The surface projections of the vertical cross-sections shown below are represented by green great-circle arcs labelled A and B.

Fig. 9(a) A shows a vertical cross-section through the North American continent in which a fast anomaly extends from the surface to  $D''$ , in agreement with Grand (1994) and Grand *et al.* (1997), although our model does not show the same level of detail. The image suggests that the 670 km discontinuity does not significantly impact on flow of material between upper and lower mantle. In cross-section A, the fast anomaly progresses quasi-continuously down to the CMB. The continuity of this anomaly at depths greater than 2000 km is nevertheless limited to the latitude shown on the cross-section, as can be inferred from Fig. 5(b): the north-south-trending linear anomaly under the eastern part of North America at depths of 1600 and





Solid line: SAW24B16, Dashed line: Harvard, Dotted line: Grand

**Figure 7.** Rms velocity profiles as a function of depth for SAW24B16 (solid line) compared to two recent  $V_s$  models: Gu & Dziewonski (2000) (dashed line) and Grand (1994) (dotted line).

1900 km abruptly changes on the 2200 and 2500 km depth sections, where it appears to be confined to the region under the Gulf of Mexico.

Cross-section B in Fig. 9(a) is taken across the Peru–Chile trench and shows a fast anomaly penetrating into the lower mantle down to a depth of about 1500 km. The model also shows a thickening of the slab in the lower mantle. Both this feature and the depth extent of the slab are consistent with the model of Grand (1994). Note the fast anomaly at the western end of cross-section B on both sides of the 670 km discontinuity, in a location that does not correspond to any known active subduction.

### 3.3 West Pacific subduction

The top of Fig. 9(b) shows a horizontal cross-section of the West Pacific and Indian Ocean regions at 175 km depth. At shallow depths, the image is dominated by the signature of back-arc spreading. The slow domain in the southwest corner coincides with the Southeast Indian Ridge, and the uppermost mantle beneath India and Australia displays high velocities.

Fig. 9(b) A is a vertical cross-section of the model across the southern Kurile Islands region, displaying a subhorizontal slab sinking to the 670 km discontinuity without entering the lower mantle. This observation is consistent with  $V_p$  models derived from ISC data (Fukao *et al.* 1992; van der Hilst *et al.* 1991) and from the waveform modelling study of (Tajima & Grand 1998).

Cross-section B of Fig. 9(b) is taken across the Japan Trench. The slab appears to ‘rest’ horizontally on the discontinuity, in agreement with van der Hilst *et al.* (1991) and Fukao *et al.* (1992). The anomaly penetrates into the lower mantle at its eastern end. The amplitude of this feature is weak and may not be well resolved but it agrees qualitatively with the results of Tajima *et al.* (1998).

Cross-section C of Fig. 9(b) is taken across the Marianas trench region and suggests that slab structure might be present in the lower mantle, down to a depth of about 900 km.

In the region across the Solomon trench (Fig. 9b, D), the slab appears confined to the transition zone and the uppermost part of the lower mantle. In contrast, the section across the Tonga–Kermadec region suggests that the slab penetrates into the lower mantle (Fig. 9b, E). Continuation of the Tonga slab into the lower mantle has been observed previously (e.g. Fischer *et al.* 1991), and the structure of the slab across the 670 km discontinuity was mapped in detail by van der Hilst (1995).

In Fig. 9(b) F, we show a cross-section across the Java subduction zone. The image suggests the presence of slab in the deep mantle, in agreement with Fukao *et al.* (1992). Although this figure suggests that the slab reaches the CMB, the amplitudes below 1500 km are not significant, indicating that the depth extent of this fast anomaly may not be reliably addressed with the present model.

Fig. 10 summarizes the trend in the Western Pacific subduction in the Northern Hemisphere. The vertical cross-section represents the +1.3 per cent isocontour level of SAW24B16 at latitudes between those of Kamchatka and Java, between 400 and 1000 km depth. The model shows that penetration of the fast anomaly under the Kamchatka/Northern Kurile region (NK) into the lower mantle is interrupted beneath Japan (JAP) but resumes under Izu–Bonin (IB). A fast domain is present in the lower mantle beneath the Marianas (MAR) and Solomon (SOL), as well as Java (JAV).

So far, we have concentrated on the fast regions of the mantle. We now turn our focus to the slow anomalies in the model.

### 3.4 East Pacific

The image of the lowermost mantle under the Pacific is dominated by a broad low-velocity region. With increasing radius, this anomaly separates into two distinct domains, below the central Pacific and below the Southeast Pacific.

In Fig. 11(a), we investigate the spatial extent of this complex anomaly. In particular, we assess its interaction in the uppermost mantle at the surface with the network of ridges in the East Pacific (the East Pacific Rise, EPR, the Pacific–Antarctic Ridge, PAR, and the Chile Ridge, CR) by showing six vertical cross-sections in the region of the Pacific bounded by 45°N180° and 70°S300°. Fig. 11(a) (top) shows a horizontal cross-section of the model at 2800 km depth, including the peak anomalies mentioned above in the mid-Pacific and the Gulf of Mexico. The surface locations of hotspots are represented on the lateral section by inverted yellow triangles related in size to the hotspot buoyancy flux observed (Sleep 1990). The projection of the hotspots located at distances up to 5° away from each great circle arc is plotted on the cross-sections.

Vertical cross-section A in Fig. 11(a) is taken in the NE–SW direction, east of the negative anomaly peak in D’, cutting across the surface locations of the Marquesas and Tahiti hotspots.

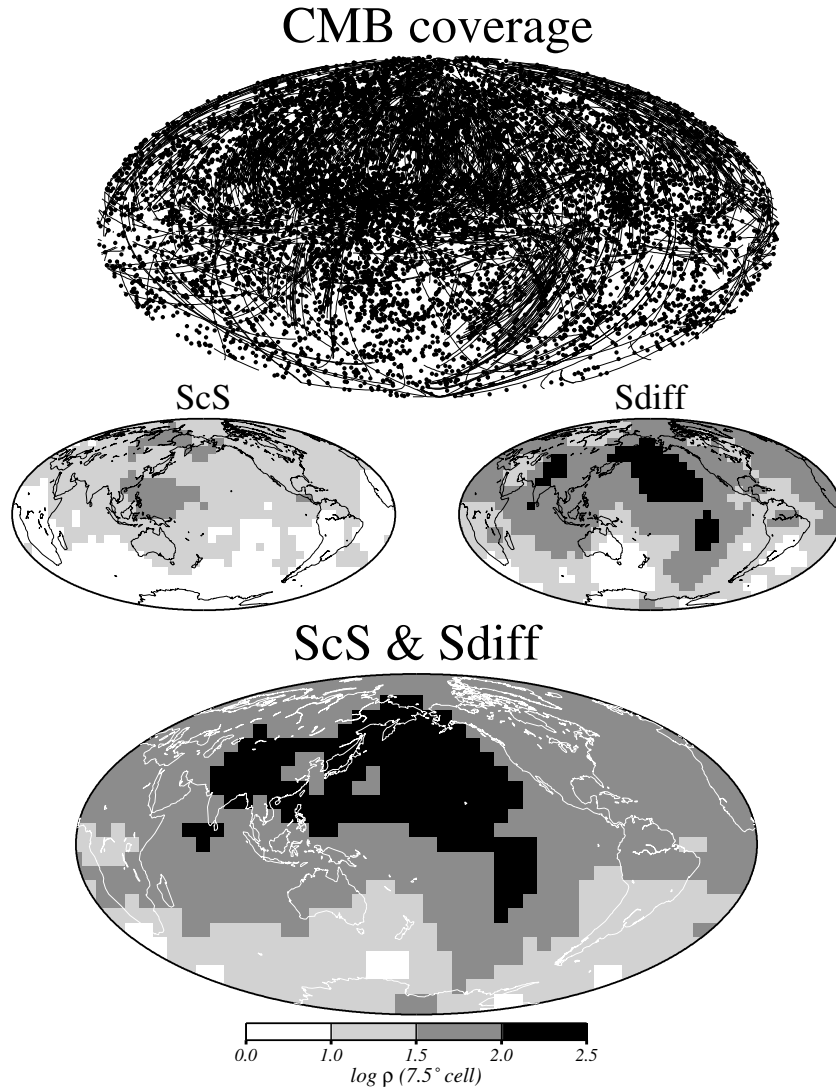


**Figure 8.** Top: projection of rays at the CMB— $S_{\text{diff}}$  and  $sS_{\text{diff}}$  (great-circle arcs),  $ScS$ ,  $ScS_2$  and  $ScS_3$  as well as corresponding depth phases (points). Middle left: density coverage ( $7.5^\circ \times 7.5^\circ$  cell) corresponding to the core-reflected phases. Middle right: density coverage ( $7.5^\circ \times 7.5^\circ$  cell) corresponding to the core-diffracted phases at the CMB. Bottom: total density coverage at the CMB.

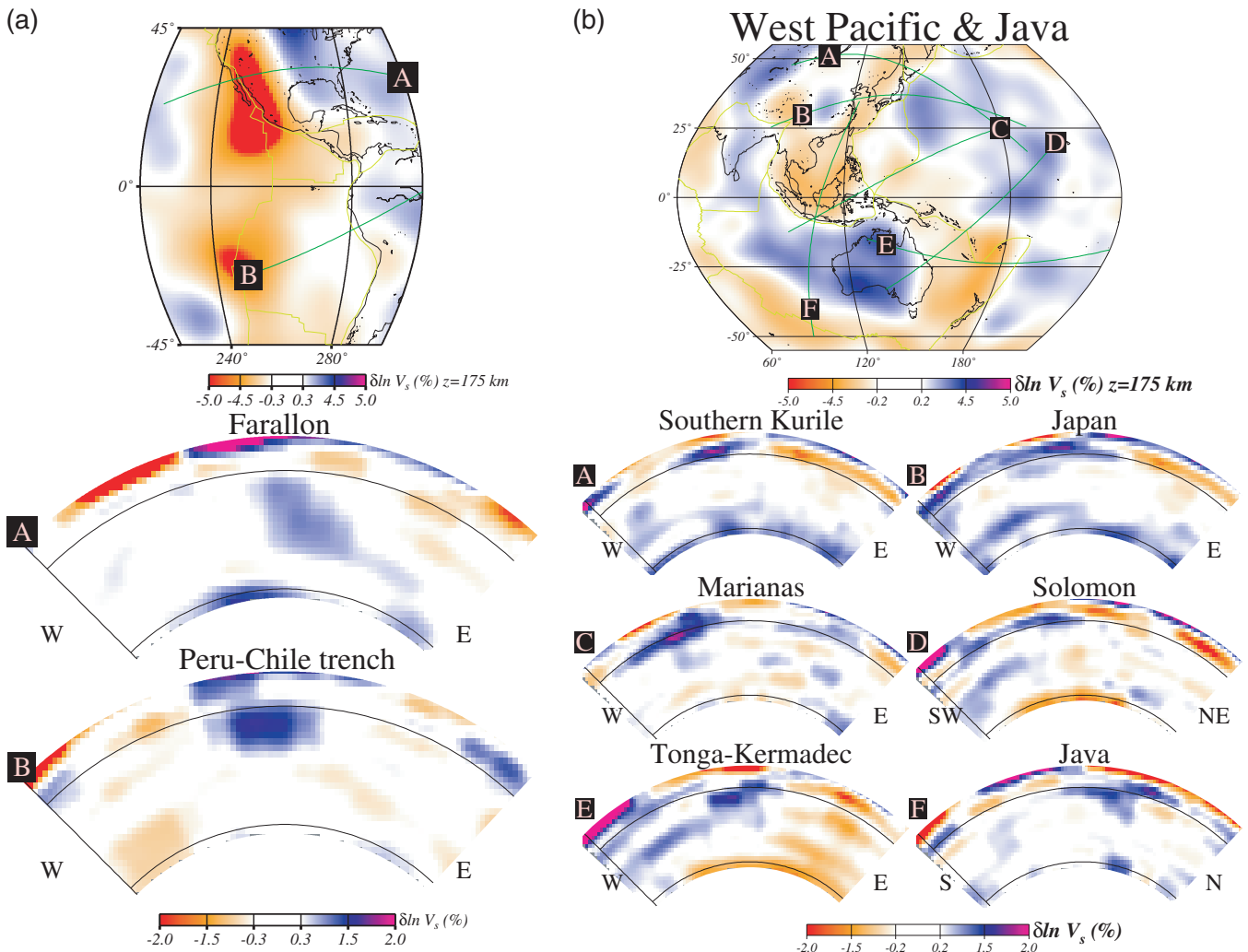
A continuous, vertically extending slow domain is observed throughout the lower mantle, spreading laterally towards the south above the 670 km discontinuity around a depth of about 450 km, south of the Tahiti hotspot. This image suggests the presence of an upwelling originating at the CMB and penetrating into the upper mantle where the red maximum ‘pools’ sideways, and connects, at the southern end, with the PAR (seen at the southern end of cross-section A in the upper mantle). It also indicates that, in the East Pacific, the 670 km discontinuity does not act as a strong barrier to upgoing flow between lower and upper mantle. We refer to this low-velocity region as ‘LOWPAC1’. This upwelling is offset to the southeast with respect to the low-velocity peak situated near the equator at  $190^\circ$  longitude.

Fig. 11(a) B is taken in the E–W direction across the Nazca Plate, showing the same slow anomaly extending from the surface location of the EPR to the top of the Great Pacific Plume LOWPAC1. The apparent shift of this anomaly is also apparent in the lateral sections of Fig. 5(a) between 100 and 525 km, where the slow region below the EPR is seen to

migrate westwards with depth. The cross-section cuts across or near the surface location of the Samoa, Tahiti, Austral/Cook Islands, Gambier Islands, Easter Island and San Felix hotspots and shows a possible relation between the upwelling and the four westernmost hotspots in the cross-section.

Vertical section C in Fig. 11(a) is taken along the great circle between Hawaii and the Austral/Cook Islands. A slow anomaly extending from about 1600 to 200 km depth and peaking in amplitude near 400 km is present beneath Hawaii. Here again, significant lateral extension of the slow domain is observed above the 670 km discontinuity. The anomaly at the southern end of the image corresponds to the eastern part of LOWPAC1 and extends continuously between the lowermost mantle and the Cook Islands hotspot at the surface.

Cross-section D in Fig. 11(a) is taken across the CR and the southwestern part of the EPR. In addition to a subhorizontal low-velocity anomaly in the upper mantle connecting the EPR to LOWPAC1 to the west, a second slow domain extends subvertically between the CR and the lowermost mantle. This smaller upwelling displays less continuity and smaller amplitudes



**Figure 9.** (a) Subduction under the Americas. Top: lateral section at 175 km depth. Bottom: depth cross-sections. A: Farallon section; B: South American section (horizontal lines correspond to 670 and 2650 km depth). (b) West Pacific and Java subduction. Top: lateral section at 175 km. Depth cross-sections A: Kurile; B: Japan; C: Marianas; D: Solomon Islands; E: Tonga–Kermadec; F: Java.

than LOWPAC1. We interpret this anomaly as being caused by a second upwelling in the Pacific and refer to it as ‘LOWPAC2’. In Fig. 11(a) E, we show the latitudinal extent of LOWPAC2 by taking a N–S section across the Nazca plate.

A cross-section along the EPR is taken in Fig. 11(a) F. Bearing in mind that the spline node spacing just above the transition zone is 150 km, the low velocity associated with the ridge is observed down to a depth of about 400 km.

Although the cross-sections show no systematic relationship between the Pacific upwellings and the surface locations of hotspots, at least two Pacific hotspots are situated at the surface end of broad negative anomalies. The Cook/Austral Islands hotspot is situated in the continuity of a low-velocity zone continuous between the CMB and the surface (southernmost hotspot in Fig. 11a, C), and Hawaii is situated at the northern end of an anomaly that extends from about 1600 to 200 km (northernmost hotspot in Fig. 11a, C).

Fig. 12 shows the  $-1.8$  per cent isocontours in the Pacific between 400 and 1000 km depth. Because the perspective is from the top, the plot represents the radially integrated structure (from 400 to 1000 km) for anomalies slower than  $-1.8$  per cent. The surface location of hotspots is represented

by circles on the plot. Close proximity is observed between the slow isocontours in the model and the surface locations of Hawaii (H), the Caroline Islands (C), Tahiti/Society Islands (S), Tasmania (T), the Austral/Cook Islands (A), Gambier (G) and West of Bowie (B). This view must be moderated by the observation that two strong low-velocity anomalies that do not coincide with hotspot locations are also present in the Pacific (east of the Kuriles and south of Gambier).

### 3.5 African upwelling

Fig. 11(b) (top) shows a lateral section of the upper mantle at 175 km depth under Africa and the Indian Ocean, displaying slow anomalies near the East African rift zone, the Red Sea and along the Mid-Indian Ridge. The East African, West African and Congo cratons are isolated by the presence of slow regions surrounding them.

Fig. 11(b) A shows a vertical SW–NE cross-section across the continent. The slow domain under Africa extends vertically from the base of the mantle into the upper mantle and is subsequently shifted to the northeast. Fig. 11(b) B shows an E–W cross-section. In the upper mantle, the low-velocity zone

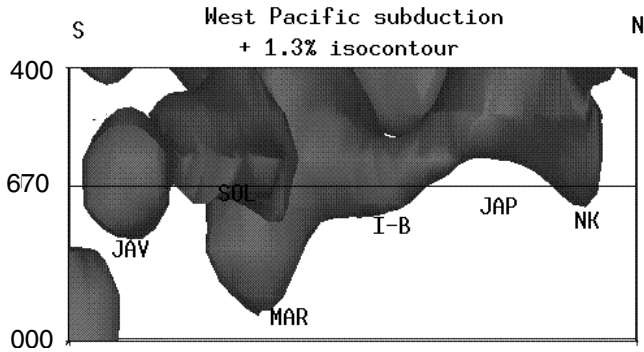
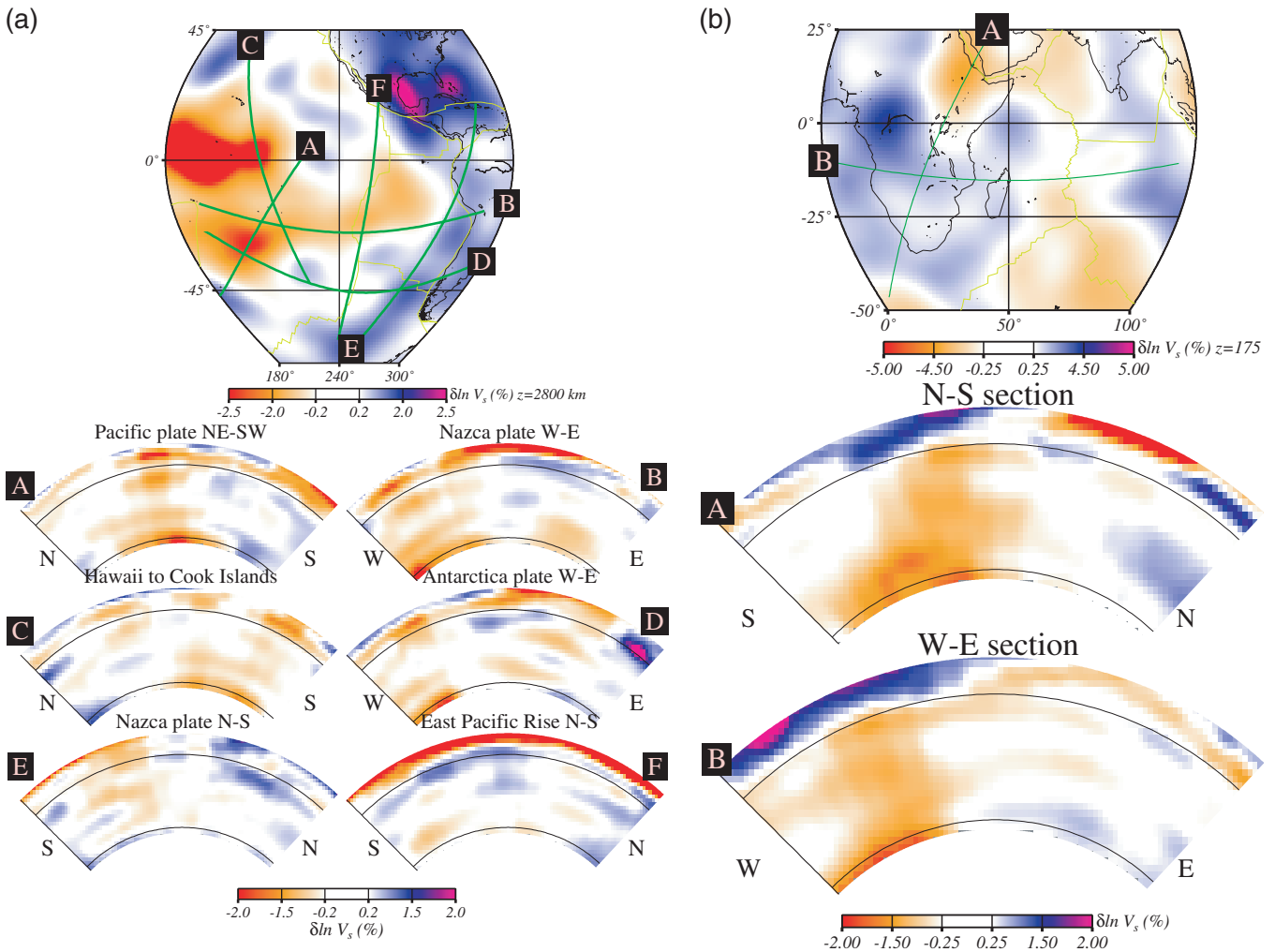


**Figure 10.** 3-D view of subduction in the Northwest Pacific. The vertical section represents the +1.3 per cent isocontour traced in the model at depths between 400 and 1000 km at latitudes between those of Kamchatka and Java. JAV = Java, SOL = Solomon, MAR = Marianas, I-B = Izu-Bonin, JAP = Japan, NK = Northern Kuriles.

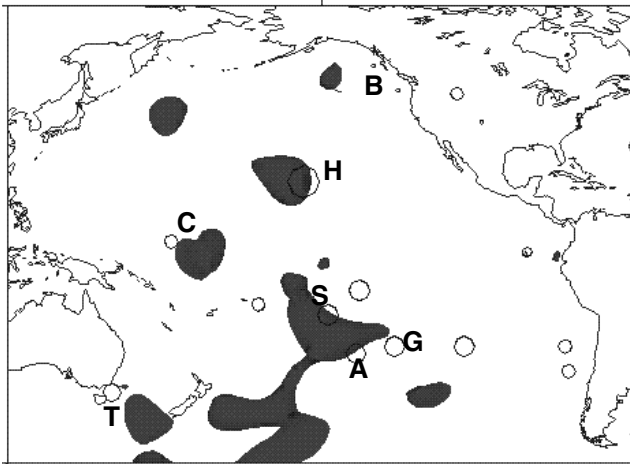
is deflected to the east by the African plate towards the Mid-Indian Ridge, with which it seems to connect. The shape of this upwelling is better seen in Fig. 13. It consists of a narrow conduit emerging from a broad base and penetrating into the upper mantle without significantly altering its shape as it

crosses 670 km. The margins and amplitude of this anomaly were investigated in a study by Ritsema *et al.* (1998), in which the amplitude and the shape of the anomaly was adjusted to satisfy *S*, *SKS*, *ScS-S* and *S-SKS* traveltimes. Cross-section A of Fig. 11(b) corresponds roughly to the great-circle path in their Fig. 1. In the lower mantle, the shape of the anomaly in SAW24B16 is in general agreement with their model M2, suggesting an upwelling shifting towards the northeast with increasing radius. However, in contrast to their study, we find continuity of the slow domain into the upper mantle. Our model displays significantly lower amplitudes than M2, peaking at about -2.6 per cent at the bottom of the mantle, and remaining constant at about -1 per cent in the rest of the lower mantle. It is, however, well known that amplitudes resulting from tomographic inversions are attenuated as a result of damping (e.g. Bréger & Romanowicz 1998).

Fig. 13 shows the isocontours corresponding to -1 per cent velocity perturbations from PREM in SAW24B16. The plot extends from 100 to 2850 km and is truncated at latitudes above 60°N and below 60°S to avoid artefacts near the poles caused by the cylindrical projection. The figure shows a large-scale low-velocity zone spread horizontally throughout the mid-Pacific at lowermost mantle depths and extending vertically in



**Figure 11.** (a) East Pacific Rise. Top: lateral section about the East Pacific Rise at 2800 km. Depth cross-sections A: Cocos plate, E-W section; B: Nazca Plate, E-W section; C: Antarctica Plate, E-W section; D: Pacific Plate, N-S section; E: Nazca plate, N-S section; F: Along-ridge section: East Pacific Rise (N-S). (b) African superswell. Top: lateral section at 175 km depth. Depth cross-sections A: N-S section; B: E-W section.

**-1.8% isocontour**

400-1000 km

**Figure 12.**  $-1.8$  per cent isocontour map in the Pacific between 400 and 1000 km depth. Because the perspective is from above, the anomalies are collapsed at the Earth's surface. The hotspots are annotated on the map as B: Bowie, H: Hawaii, C: Caroline islands, S: Society islands, A: Austral/Cook Islands, G: Gambier, T: Tasmania. The perspective is from the top, showing the projection of all negative anomalies  $\delta V_{sh} \leq 1.8$  per cent between 400 and 1000 km depth onto the surface of the Earth.

the mid-Pacific. The slow domain in the mid-Pacific corresponds to LOWPAC1 and is reminiscent of the characteristic shape of a plume (e.g. Olson *et al.* 1993), with a large-scale base overlain by a narrow conduit topped in turn by a broad 'head'. The narrowing of the slow anomaly with radius is in agreement with the study of Bréger & Romanowicz (1998). The anomaly LOWPAC2 originates at the southeastern end of the basal feature at the CMB. At the western part of the plot, the anomaly under Africa is also characterized by a large-scale domain at the bottom of the mantle, narrowing with increasing radius.

#### 4 DISCUSSION

Two slow regions, originating beneath Africa and the Pacific in the lower mantle and extending into the uppermost mantle, are present in every published model of the whole mantle (e.g. Liu & Dziewonski 1998; Masters *et al.* 1996; Grand 1994; Su *et al.* 1994) and usually interpreted as a superplume. In this study, we suggest that there may exist two distinct upwellings under the Pacific, each displaying some level of interaction with the

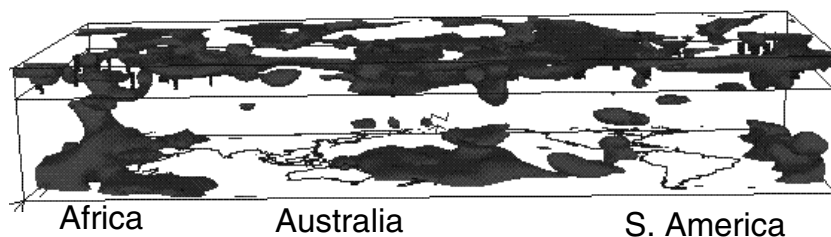
complex of ridges at uppermost mantle depths. A low-velocity anomaly 'LOWPAC1' is centred around  $20^\circ\text{S}$ ,  $160^\circ\text{W}$  extending vertically to 450 km depth where it pools laterally and joins the Pacific–Antarctic Ridge to the south and the East Pacific Rise to the east. LOWPAC1 continues its ascension vertically into the upper mantle at its eastern end, where it coincides with the Austral/Cook hotspot region. A second anomaly, 'LOWPAC2', can be traced from the CMB near  $45^\circ\text{S}$ ,  $80^\circ\text{W}$  subvertically to the Chile Ridge.

The African upwelling appears to separate laterally beneath the thick fast anomaly beneath Africa to join the Mid-Atlantic Ridge to the west and the Mid-Indian Ridge to the east. The multiplicity of ridge–plume interactions may not be fortuitous: based on a study of the distribution of hotspots at plate boundaries, Weinstein & Olson (1989) demonstrated the high statistical significance of the presence of hotspots near divergent margins and hypothesized that it is the result of a plume capture effect caused by the upward flow in the vicinity of the spreading centres. This effect is also observed in convection simulations (e.g. Steinberger & O'Connell 1998).

Localized negative peaks in velocity coincide at upper mantle depths with the surface locations of many hotspots. Plumes are considered to be much finer features than can be resolved at degree 24, but with the caveat that there also exist high negative-amplitude peaks in the model that do not correspond to hotspots, the tomographic image may represent the smeared version of such anomalies.

A phase transition with a negative Clapeyron slope is expected to slow down the progression of cold downwellings and hot upwellings due to the restoring force that opposes the boundary deflection. In tomographic images, such a barrier would manifest itself by lateral pooling of heterogeneity near the discontinuity. In Fig. 14 (top), we plot isocontours of the  $-1.25$  per cent level in SAW24B16 between 400 and 1000 km depth. The perspective is from the south looking towards the north. The image shows that the shape of the slow anomalies is unaffected by the transition into the upper mantle. It is, however, possible that the continuity of the model anomalies between the upper and the lower mantle is an artefact caused by the adoption of a continuous parametrization across the discontinuity at 670 km. Fig. 14 (bottom) shows the 1 per cent isocontour in model SAW12D (Li & Romanowicz 1996) from the same visual perspective. SAW12D was computed using two sets of Legendre polynomials for the radial parametrization, decoupled at 670 km. Here again, we observe continuity of the slow anomalies across the transition from upper to lower mantle, in spite of the split parametrization.

Continuity between the upper and the lower mantle is also observed in most regions of subduction, except in the

**-1% isocontour**

**Figure 13.** Whole-mantle  $-1$  per cent isocontour level in model SAW24B16 between the surface and the CMB. Only latitudes between  $60^\circ\text{N}$  and  $60^\circ\text{S}$  are shown to avoid the artefacts caused by the cylindrical projection near the poles.

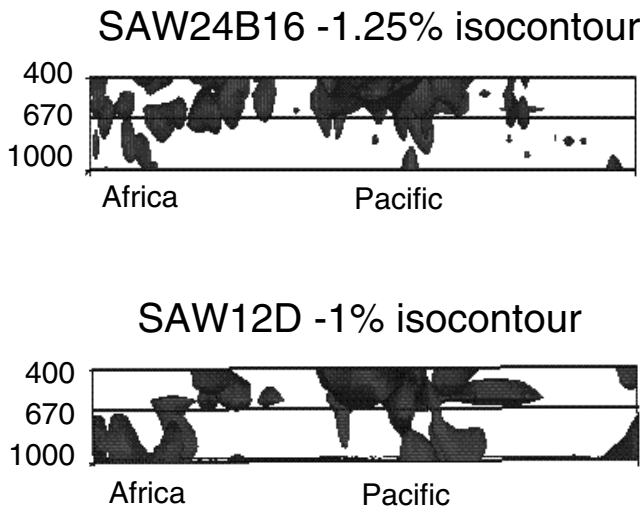


**Figure 14.** Isocontour levels in the whole mantle between 400 and 1000 km depth. The perspective of the each vertical section is taken from the south looking northwards. Top:  $-1.25$  per cent isocontour level for model SAW24B16. The radial parametrization is continuous across the 670 km discontinuity. Bottom:  $-1$  per cent isocontour level for model SAW12D. The parametrization is split across the 670 km discontinuity.

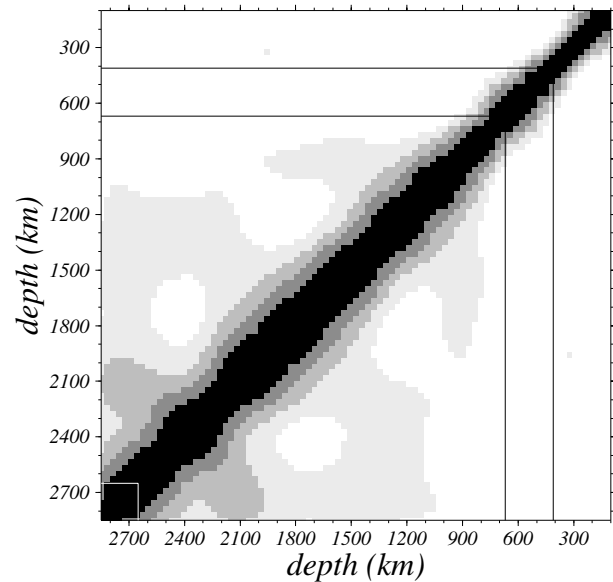
Northwestern Pacific between the Southern Kuriles and Izu, where the slab deflection has been hypothesized to be the result of the oceanward motion of the trench with age (van der Hilst & Seno 1993).

Another seismological diagnostic of the slowing of flow across the mantle is the analysis of the correlation of the seismic velocity field with itself across the discontinuity (Jordan *et al.* 1993). In Fig. 15 (top), we plot the radial correlation function for SAW24B16 and compare it with that of a 3-D spherical convection calculation including phase transitions at 410 and 670 km depth (Bunge *et al.* 1998). The convection model shows a strong ‘pinching’ of the correlation field at 670 km where the endothermic phase transition is imposed. We have shown in two recent studies (Mégnin & Romanowicz 2000; Mégnin *et al.* 1997) that such features would be resolved in the tomography. Narrowing of the correlation band across the boundary between upper and lower mantle is not observed here, further suggesting that the phase transition at 670 km does not significantly impede flow between upper and lower mantle. In contrast, the progression with depth of many slabs, as well as the ‘pinching’ of LOWPAC1 in the Central Pacific and of the African plume a few hundred kilometres above their bases, as displayed in Fig. 13, may suggest that other barriers to flow, possibly caused by compositional layering, may be present deeper in the mantle (e.g. van der Hilst & Kárason 1999; Kellogg *et al.* 1999), but not as high above the CMB as suggested by these authors.

#### ACKNOWLEDGMENTS

We thank Raphaelle Millot and Sean Ford for their help with the collection of data, Ludovic Bréger for his body wave sampling code, and the staff of the IRIS and GEOSCOPE networks for making the data available. We are indebted to Xiang-Dong Li for collecting the greatest part of the data and developing critical portions of the software used in this study. Thanks also to Philip B. Stark for a thorough reading

#### Radial correlation functions SAW24B16



#### GEMLAB1

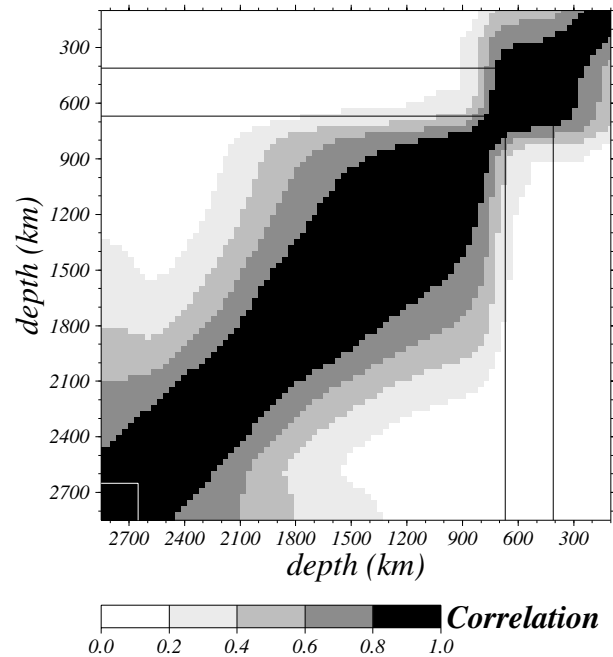


**Figure 15.** Top: radial correlation function (RCF) for SAW24B16. Bottom: RCF of the convection model GEMLAB1 (Bunge *et al.* 1998).

of the manuscript. All figures were generated using GMT (Wessel & Smith 1991), except Figs 10, 12, 13 and 14, which were created with VIS5D (Hibbard & Santek 1990). The model SAW24B16 is available by anonymous ftp from the site [quake.geo.berkeley.edu/pub/saw/saw24b16.tar.gz](http://quake.geo.berkeley.edu/pub/saw/saw24b16.tar.gz) and at the URL <http://www.seismo.berkeley.edu/pepe/saw24b16.html>.

#### REFERENCES

- Bijwaard, H., Spakman, W. & Engdahl, R., 1998. Closing the gap between regional and global traveltimes tomography, *J. geophys. Res.*, **103**, 30 055–30 078.

- Bréger, L. & Romanowicz, B., 1998. Test of tomographic models of D' using differential travel time data, *Science*, **282**, 718–720.
- Bunge, H.-P., Richards, M.A., Lithgow-Bertelloni, C., Baumgardner, J.R., Grand, S.P. & Romanowicz, B., 1998. Time scales and heterogeneous structure in geodynamic earth models, *Science*, **280**, 91–95.
- De Boor, C., 1978. *A Practical Guide to Splines*, Springer-Verlag, New York.
- Ding, X.Y. & Grand, S.P., 1994. Seismic structure of the deep kurile subduction zone, *J. geophys. Res.*, **99**, 23 767–23 786.
- Durek, J.J. & Ekström, G., 1996. A radial model of anelasticity consistent with long period surface wave attenuation, *Bull. seism. Soc. Am.*, **86**, 144–158.
- Dziewonski, A.M. & Anderson, D.L., 1981. Preliminary reference Earth model, *Phys. Earth planet. Inter.*, **25**, 297–356.
- Dziewonski, A.M., Hager, B.H. & O'Connell, R.J., 1977. Large scale heterogeneities in the lower mantle, *J. geophys. Res.*, **82**, 297–356.
- Edmonds, A.R., 1960. *Angular Momentum in Quantum Mechanics*, Princeton University Press, Princeton, NJ.
- Engdahl, E.R., van der Hilst, R.D. & Buland, R.P., 1998. Global teleseismic earthquake relocation with improved travel times and procedures for depth determination, *Bull. seism. Soc. Am.*, **88**, 722–743.
- ETOPO-5, 1990. Data announcement, 88-mgg-02, digital relief of the surface of the earth, *Tech. Rept.*, NOAA, National Geophysical Data Center, Boulder, CO.
- Fischer, K.M., Creager, K.C. & Jordan, T.H., 1991. Mapping the Tonga slab, *J. geophys. Res.*, **96**, 14 403–14 427.
- Fukao, Y., Obayashi, M., Inoue, H. & Nenbai, M., 1992. Subducting slabs stagnant in the mantle transition zone, *J. geophys. Res.*, **97**, 4809–4822.
- Grand, S.P., 1994. Mantle shear structure beneath the Americas and surrounding oceans, *J. geophys. Res.*, **99**, 11 591–11 621.
- Grand, S.P., van der Hilst, R.D. & Widiyantoro, S., 1997. Global seismic tomography: a snapshot of convection in the earth, *Geol. Soc. Am. Today*, **7**, 1–7.
- Gu, L. & Dziewonski, A.M., 2000. Shear velocity of the mantle and discontinuities in the pattern of lateral heterogeneities, *J. geophys. Res.*, submitted.
- Hibbard, W. & Santek, D., 1990. The vis5d system for easy interactive visualization, in *Proc. Visualization '90*, pp. 28–35, IEEE, San Francisco, CA.
- Jackson, D.D., 1979. The use of a priori data to resolve non-uniqueness in linear inversion, *Geophys. J. R. astr. Soc.*, **57**, 137–157.
- Jordan, T.H., Puster, P., Glatzmaier, G.A. & Tackley, P.J., 1993. Comparisons between seismic earth structures and mantle flow models based on radial correlation functions, *Science*, **261**, 1427–1431.
- Kellogg, L.H., Hager, B.H. & van der Hilst, R.D., 1999. Compositional stratification in the deep mantle, *Science*, **283**, 1881–1884.
- Li, X.D. & Romanowicz, B., 1995. Comparison of global waveform inversions with and without considering cross-branch modal coupling, *Geophys. J. Int.*, **121**, 695–709.
- Li, X.D. & Romanowicz, B., 1996. Global mantle shear-velocity model developed using nonlinear asymptotic coupling theory, *J. geophys. Res.*, **101**, 22 245–22 272.
- Li, X.D. & Tanimoto, T., 1993. Waveforms of long-period body waves in a slightly aspherical earth model, *Geophys. J. R. astr. Soc.*, **112**, 92–102.
- Liu, X.-F. & Dziewonski, A.M., 1994. Lowermost mantle shear wave velocity structure, *EOS, Trans. Am. geophys. Un.*, **78**, 663.
- Liu, X.-F. & Dziewonski, A.M., 1998. Global analysis of shear wave velocity anomalies in the lower-most mantle, in *Core-mantle boundary region*, Vol. 28, pp. 21–36, eds Wyssession, T.E., Knittle, E. & Buffett, B., G.M., AGU, Washington, DC.
- Marquering, H. & Snieder, R., 1995. Surface wave mode coupling for efficient forward modelling and inversion of body-wave phases, *Geophys. J. Int.*, **120**, 186–208.
- Masters, G., Johnson, S., Laske, G. & Bolton, H., 1996. A shear-velocity model of the mantle, *Phil. Trans. R. Soc. Lond.*, **A354**, 1385–1410.
- Mégnin, C. & Romanowicz, B., 1999. The effects of the theoretical formalism and data selection on mantle models derived from waveform tomography, *Geophys. J. Int.*, **138**, 366–380.
- Mégnin, C. & Romanowicz, B., 2000. A comparison between tomographic and geodynamic models of the earth's mantle, in *Dynamics of Plate Motions*, ed. van der Hilst, R.D., AGU, Washington, DC, in press.
- Mégnin, C., Bunge, H.-P., Romanowicz, B. & Richards, M.A., 1997. Imaging 3-D spherical convection models: what can seismic tomography tell us about mantle dynamics?, *Geophys. Res. Lett.*, **24**, 1299–1303.
- Michellini, A. & McEvelly, T.V., 1991. Seismological studies at Parkfield. I. Simultaneous inversion for velocity structure and hypocenters using b-splines parametrization, *Bull. seism. Soc. Am.*, **81**, 524–552.
- Nataf, H.-C., Nakanishi, I. & Anderson, D.L., 1986. Measurements of mantle wave velocities and inversion for lateral heterogeneities and anisotropy, *J. geophys. Res.*, **91**, 7261–7307.
- Olson, P.L., Schubert, G. & Anderson, C., 1993. Structure of axisymmetric mantle plumes, *J. geophys. Res.*, **98**, 6829–6844.
- Park, J., 1987. Asymptotic coupled mode expressions for multiplet amplitude anomalies and frequency shifts on an aspherical earth, *Geophys. J. R. astr. Soc.*, **90**, 129–169.
- Press, W.H., Teukolsky, S.A., Vetterling, W.T. & Flannery, B.P., 1994. *Numerical Recipes in C*, 2nd edn, Cambridge University Press, Cambridge, MA.
- Resovsky, J.S. & Ritzwoller, M.H., 1999. A degree 8 mantle shear velocity model from normal mode observations below 3 mHz, *J. geophys. Res.*, **104**, 993–1014.
- Ritsema, J., Ni, S., Helmberger, D.V. & Crotwell, H.P., 1998. Evidence for strong shear velocity reductions and velocity gradients in the lower mantle beneath africa, *Geophys. Res. Lett.*, **25**, 4245–4248.
- Romanowicz, B., 1987. Multiplet–multiplet coupling due to lateral heterogeneity: asymptotic effects on the amplitude and frequency of earth's normal modes, *Geophys. J. R. astr. Soc.*, **90**, 75–100.
- Sleep, N.H., 1990. Hotspots and mantle plumes: some phenomenology, *J. geophys. Res.*, **95**, 6715–6736.
- Steinberger, B. & O'Connell, R.J., 1998. Advection of plumes in mantle flow: implications for hotspot motion, mantle viscosity and plume distribution, *Geophys. J. Int.*, **132**, 412–434.
- Stutzmann, E. & Montagner, J.-P., 1993. An inverse technique for retrieving higher mode phase velocity and mantle structure, *Geophys. J. Int.*, **113**, 669–683.
- Stutzmann, E. & Montagner, J.-P., 1994. Tomography of the transition zone from the inversion of higher mode surface waves, *Phys. Earth planet. Inter.*, **86**, 99–115.
- Su, W.J. & Dziewonski, A.M., 1996. Global tomographic inversion using b-splines, *EOS, Trans. Am. geophys. Un.*, **77**, 46.
- Su, W.J., Woodward, R.L. & Dziewonski, A.M., 1994. Degree 12 model of shear velocity in the mantle, *J. geophys. Res.*, **352**, 6945–6980.
- Tajima, F. & Grand, S.P., 1998. Variation of transition zone high-velocity anomalies and depression of 660 km discontinuity associated with subduction zones from the southern Kuriles to Izu-Bonin and Ryukyu, *J. geophys. Res.*, **103**, 15 015–15 036.
- Tajima, F., Fukao, Y., Obayashi, M. & Sakurai, T., 1998. Evaluation of slab images in the northwestern Pacific, *Earth Planets Space*, **50**, 953–964.
- Takeuchi, H. & Saito, M., 1972. Seismic surface waves, *Methods Comput. Phys.*, **11**, 217–295.
- Tanimoto, T., 1984. A simple derivation of the formula to calculate synthetic long-period seismograms in a heterogeneous earth by normal mode summation, *Geophys. J. R. astr. Soc.*, **77**, 275–278.
- Tanimoto, T., 1989. The three-dimensional shear wave structure in the mantle by overtone waveform inversion—I. Radial seismogram inversion, *Geophys. J. R. astr. Soc.*, **89**, 713–740.

- Tarantola, A. & Valette, B., 1982. Generalized non-linear inverse problems solved using the least-squares criterion, *Rev. Geophys. Space Phys.*, **20**, 219–232.
- van der Hilst, R.D., 1995. Complex morphology of subducted lithosphere in the mantle beneath the tonga trench, *Nature*, **374**, 154–157.
- van der Hilst, R.D. & Kárason, H., 1999. Compositional heterogeneity in the bottom 1000 kilometers of the mantle: toward a hybrid convection model, *Science*, **283**, 1885–1888.
- van der Hilst, R.D. & Seno, T., 1993. Effects of relative plate motion on the deep structure and penetration depth of slabs below the Izu-Bonin and Mariana arcs, *Earth planet. Sci. Lett.*, **120**, 395–407.
- van der Hilst, R.D., Engdahl, E.R., Spakman, W. & Nolet, G., 1991. Tomographic imaging of subducted lithosphere below northwest Pacific island arcs, *Nature*, **353**, 37–42.
- van der Hilst, R.D., Widiyantoro, S. & Engdahl, E.R., 1997. Evidence of deep mantle circulation from global tomography, *Nature*, **386**, 578–584.
- van der Lee, S. & Nolet, G., 1997. Upper mantle s velocity structure of North America, *J. geophys. Res.*, **102**, 22 815–22 838.
- van Heijst, H.J. & Woodhouse, J.H., 1997. Measuring surface wave overtone phase velocities using a mode branch stripping technique, *Geophys. J. Int.*, **131**, 209–230.
- van Heijst, H.J. & Woodhouse, J.H., 1999. Global high-resolution phase velocity distributions of overtone and fundamental-mode surface waves determined by mode branch stripping, *Geophys. J. Int.*, **137**, 601–620.
- Vasco, D.W. & Johnson, L.R., 1998. Whole earth structure estimated from seismic arrival times, *J. geophys. Res.*, **103**, 2633–2671.
- Vasco, D.W., Johnson, L.R., Pulliam, R.J. & Earle, P.S., 1994. Robust inversion of iasp91 travel time residuals for mantle P and S velocity structure, earthquake mislocations and station corrections, *J. geophys. Res.*, **99**, 13 727–13 755.
- Wang, Z. & Dahlen, F.A., 1995. Spherical spline parametrization of three-dimensional earth models, *Geophys. Res. Lett.*, **22**, 3099–3102.
- Wang, Z., Tromp, J. & Ekström, G., 1998. Global and regional surface-wave inversions; a spherical-spline parameterization, *Geophys. Res. Lett.*, **25**, 207–210.
- Weinstein, S.A. & Olson, P.L., 1989. The proximity of hotspots to convergent and divergent plate boundaries, *Geophys. Res. Lett.*, **16**, 433–436.
- Wessel, P. & Smith, W.H.F., 1991. New version of the Generic Mapping Tool released, *EOS, Trans. Am. geophys. Un.*, **72**, 441, 445–446.
- Woodhouse, J.H., 1983. The joint inversion of seismic waveforms for lateral variations in earth structure and earthquake source parameters, in *Earthquakes: Observations, Theory and Interpretation*, pp. 366–397, eds Kanamori, H. & Boschi, E., North-Holland, Amsterdam.
- Woodhouse, J.H. & Dziewonski, A.M., 1984. Mapping the upper mantle: three dimensional modeling of Earth's structure by inversion of seismic waveforms, *J. geophys. Res.*, **89**, 5953–5986.

## APPENDIX A: CONSTRUCTION OF THE CUBIC B-SPLINES

We construct the set of  $N$  cubic b-spline basis functions  $B_0(r)$  to  $B_{N-1}(r)$  (e.g. De Boor 1978) following the approach of Michelini & McEvelly (1991). Their formalism was, however, developed for equidistant spline knots. For the purpose of this study, we generalize their approach to the case of arbitrarily spaced splines and impose unit area under each spline.

### A1 General case

Cubic b-splines  $B_k(r)$  whose knots are placed at a distance greater than two knots away from the edges ( $2 \leq k \leq N-3$ ) are constructed as the sum of four cubic polynomials,  ${}_k\rho_j$ , on the interval between  $r_{k-2}$  and  $r_{k+2}$ :

$$B_k(r) = \sum_{j=0}^3 {}_k\rho_j(r), \quad (\text{A1})$$

where the polynomials are defined as

$${}_k\rho_j(r) = a_j^k(r - r_j)^3 + b_j^k(r - r_j)^2 + c_j^k(r - r_j) + d_j^k, \quad (\text{A2})$$

$$r_{k-2+j} < r < r_{k-1+j}, \quad {}_k\rho_j(r) = 0 \quad \text{elsewhere.} \quad (\text{A3})$$

The 16 coefficients  $a_j^k$ ,  $b_j^k$ ,  $c_j^k$  and  $d_j^k$  are determined by imposing the following conditions.

- (i) The spline function and its first and second derivatives vanish at the endpoints (six conditions):

$${}_k\rho_0(r_{k-2}) = {}_k\rho'_0(r_{k-2}) = {}_k\rho''_0(r_{k-2}) = 0,$$

$${}_k\rho_0(r_{k+2}) = {}_k\rho'_0(r_{k+2}) = {}_k\rho''_0(r_{k+2}) = 0.$$

- (ii) Continuity of the spline and its first and second derivatives (nine conditions):

$${}_k\rho_0(r_{k-1}) = {}_k\rho_1(r_{k-1}); \quad {}_k\rho_1(r_k) = {}_k\rho_2(r_k); \quad {}_k\rho_2(r_{k+1}) = {}_k\rho_3(r_{k+1}),$$

$${}_k\rho'_0(r_{k-1}) = {}_k\rho'_1(r_{k-1}); \quad {}_k\rho'_1(r_k) = {}_k\rho'_2(r_k); \quad {}_k\rho'_2(r_{k+1}) = {}_k\rho'_3(r_{k+1}),$$

$${}_k\rho''_0(r_{k-1}) = {}_k\rho''_1(r_{k-1}); \quad {}_k\rho''_1(r_k) = {}_k\rho''_2(r_k); \quad {}_k\rho''_2(r_{k+1}) = {}_k\rho''_3(r_{k+1}).$$



(iii) Normalization condition:

$$\int_{r_{k-2}}^{r_{k+2}} B_k(r) dr = 1.$$

The solution of the  $16 \times 16$  linear system yields the following values for the unknown coefficients:

$$d_0^k = \frac{4}{h_0(h_0 + h_1)(h_0 + h_1 + h_2)(h_0 + h_1 + h_2 + h_3)},$$

$$b_0^k = c_0^k = d_0^k = 0,$$

$$d_1^k = \frac{-4(h_0^2 + 3h_0h_1 + 3h_1^2 + 2h_0h_2 + 4h_1h_2 + h_2^2 + h_0h_3 + 2h_1h_3 + h_2h_3)}{h_1(h_0 + h_1)(h_1 + h_2)(h_0 + h_1 + h_2)(h_1 + h_2 + h_3)(h_0 + h_1 + h_2 + h_3)},$$

$$b_1^k = \frac{12}{(h_0 + h_1)(h_0 + h_1 + h_2)(h_0 + h_1 + h_2 + h_3)},$$

$$c_1^k = \frac{12h_0}{(h_0 + h_1)(h_0 + h_1 + h_2)(h_0 + h_1 + h_2 + h_3)},$$

$$d_1^k = \frac{4h_0^2}{(h_0 + h_1)(h_0 + h_1 + h_2)(h_0 + h_1 + h_2 + h_3)},$$

$$d_2^k = \frac{4(h_0h_1 + h_1^2 + 2h_0h_2 + 4h_1h_2 + 3h_2^2 + h_0h_3 + 2h_1h_3 + 3h_2h_3 + h_3^2)}{h_2(h_1 + h_2)(h_0 + h_1 + h_2)(h_2 + h_3)(h_1 + h_2 + h_3)(h_0 + h_1 + h_2 + h_3)},$$

$$b_2^k = \frac{-12(h_0 + 2h_1 + 2h_2 + h_3)}{(h_1 + h_2)(h_0 + h_1 + h_2)(h_1 + h_2 + h_3)(h_0 + h_1 + h_2 + h_3)},$$

$$c_2^k = \frac{12(-h_0h_1 - h_1^2 + h_2^2 + h_2h_3)}{(h_1 + h_2)(h_0 + h_1 + h_2)(h_1 + h_2 + h_3)(h_0 + h_1 + h_2 + h_3)},$$

$$d_2^k = \frac{4(2h_0h_1h_2 + 2h_1^2h_2 + h_0h_2^2 + 2h_1h_2^2 + h_0h_1h_3 + h_1^2h_3 + h_0h_2h_3 + 2h_1h_2h_3)}{(h_1 + h_2)(h_0 + h_1 + h_2)(h_1 + h_2 + h_3)(h_0 + h_1 + h_2 + h_3)},$$

$$d_3^k = \frac{-4}{h_3(h_2 + h_3)(h_1 + h_2 + h_3)(h_0 + h_1 + h_2 + h_3)},$$

$$b_3^k = \frac{12}{(h_2 + h_3)(h_1 + h_2 + h_3)(h_0 + h_1 + h_2 + h_3)},$$

$$c_3^k = \frac{-12h_3}{(h_2 + h_3)(h_1 + h_2 + h_3)(h_0 + h_1 + h_2 + h_3)},$$

$$d_3^k = \frac{4h_3^2}{(h_2 + h_3)(h_1 + h_2 + h_3)(h_0 + h_1 + h_2 + h_3)},$$

where, dropping the implicit index  $k$  for the  $h_i^k$ , we define the spacing between two adjacent knots  $h_i \equiv r_{k+i-2} - r_{k+i-1}$ .

## A2 Case $k=1$

The second b-spline  $B_1(r)$  is constructed with three cubic polynomials on the interval between  $r_0$  and  $r_3$ :

$$B_1(r) = \sum_{j=0}^2 \rho_j(r), \quad (A4)$$

$$r_j < r < r_{j+1}, \quad \rho_j(r) = 0 \quad \text{elsewhere.} \quad (A5)$$

We impose the same normalization condition as for the general case. We also retain the continuity conditions for the right-hand side but we relax the condition that the second derivative vanish on the left-hand side to avoid the trivial solution. The nine coefficients

obtained are as follows:

$$a_0^1 = \frac{-4(3h_0 + 2h_1 + h_2)}{h_0(h_0 + h_1)(h_0 + h_1 + h_2)(3h_0^2 + 4h_0h_1 + h_1^2 + 2h_0h_2 + h_1h_2)},$$

$$b_0^1 = d_0^1 = 0,$$

$$c_0^1 = \frac{12}{h_0(h_0 + h_1)(h_0 + h_1 + h_2)(3h_0^2 + 4h_0h_1 + h_1^2 + 2h_0h_2 + h_1h_2)},$$

$$a_1^1 = \frac{4(2h_0^2 + 6h_0h_1 + 3h_1^2 + 3h_0h_2 + 3h_1h_2 + h_2^2)}{h_1(h_0 + h_1)(h_1 + h_2)(h_0 + h_1 + h_2)},$$

$$b_1^1 = \frac{-12(3h_0 + 2h_1 + h_2)}{(h_0 + h_1)(h_0 + h_1 + h_2)(3h_0^2 + 4h_0h_1 + h_1^2 + 2h_0h_2 + h_1h_2)},$$

$$c_1^1 = \frac{12(-2h_0^2 + h_1^2 + h_1h_2)}{(h_0 + h_1)(h_0 + h_1 + h_2)(3h_0^2 + 4h_0h_1 + h_1^2 + 2h_0h_2 + h_1h_2)},$$

$$d_1^1 = \frac{4h_0(4h_0h_1 + 3h_1^2 + 2h_0h_2 + 3h_1h_2)}{(h_0 + h_1)(h_0 + h_1 + h_2)(3h_0^2 + 4h_0h_1 + h_1^2 + 2h_0h_2 + h_1h_2)},$$

$$a_2^1 = \frac{-4(2h_0 + h_1)}{h_2(h_1 + h_2)(h_0 + h_1 + h_2)(3h_0^2 + 4h_0h_1 + h_1^2 + 2h_0h_2 + h_1h_2)},$$

$$b_2^1 = \frac{12(2h_0 + h_1)}{(h_1 + h_2)(h_0 + h_1 + h_2)(3h_0^2 + 4h_0h_1 + h_1^2 + 2h_0h_2 + h_1h_2)},$$

$$c_2^1 = \frac{-12h_2(2h_0 + h_1)}{(h_1 + h_2)(h_0 + h_1 + h_2)(3h_0^2 + 4h_0h_1 + h_1^2 + 2h_0h_2 + h_1h_2)},$$

$$d_2^1 = \frac{4h_2^2(2h_0 + h_1)}{(h_1 + h_2)(h_0 + h_1 + h_2)(3h_0^2 + 4h_0h_1 + h_1^2 + 2h_0h_2 + h_1h_2)}.$$

### A3 Case $k = N - 2$

The penultimate b-spline  $B_{N-2}(r)$  is constructed on the interval between  $r_{N-4}$  and  $r_{N-1}$ :

$$B_{(N-2)}(r) = \sum_{j=0}^2 (N-2)\rho_j(r), \quad (\text{A6})$$

$$r_{N+j-2} < r < r_{N+j-1}, \quad (N-2)\rho_j(r) = 0 \quad \text{elsewhere.} \quad (\text{A7})$$

We keep the same normalization and, interverting the right-hand side and left-hand side, we use the continuity conditions as for the case  $k=1$ . The solution of the  $9 \times 9$  system yields

$$a_0^{N-2} = \frac{4(h_1 + 2h_2)}{h_0(h_0 + h_1)(h_0 + h_1 + h_2)(h_0h_1 + h_1^2 + 2h_0h_2 + 4h_1h_2 + 3h_2^2)},$$

$$b_0^{N-2} = c_0^{N-2} = d_0^{N-2} = 0,$$

$$a_1^{N-2} = \frac{-4(h_0^2 + 3h_0h_1 + 3h_1^2 + 3h_0h_2 + 6h_1h_2 + 2h_2^2)}{h_1(h_0 + h_1)(h_1 + h_2)(h_0h_1 + h_1^2 + 2h_0h_2 + 4h_1h_2 + 3h_2^2)},$$

$$b_1^{N-2} = \frac{12(h_1 + 2h_2)}{(h_0 + h_1)(h_0 + h_1 + h_2)(h_0h_1 + h_1^2 + 2h_0h_2 + 4h_1h_2 + 3h_2^2)},$$

$$c_1^{N-2} = \frac{12h_0(h_1 + 2h_2)}{(h_0 + h_1)(h_0 + h_1 + h_2)(h_0h_1 + h_1^2 + 2h_0h_2 + 4h_1h_2 + 3h_2^2)},$$

$$d_1^{N-2} = \frac{4h_0^2(h_1 + 2h_2)}{(h_0 + h_1)(h_0 + h_1 + h_2)(h_0h_1 + h_1^2 + 2h_0h_2 + 4h_1h_2 + 3h_2^2)},$$

$$a_2^{N-2} = \frac{4(h_0 + 2h_1 + 3h_2)}{h_2(h_1 + h_2)(h_0 + h_1 + h_2)(h_0h_1 + h_1^2 + 2h_0h_2 + 4h_1h_2 + 3h_2^2)},$$

$$b_2^{N-2} = \frac{-12(h_0 + 2h_1 + 3h_2)}{(h_1 + h_2)(h_0 + h_1 + h_2)(h_0h_1 + h_1^2 + 2h_0h_2 + 4h_1h_2 + 3h_2^2)},$$

$$c_2^{N-2} = \frac{12(-h_0h_1 - h_1^2 + 2h_2^2)}{(h_1 + h_2)(h_0 + h_1 + h_2)(h_0h_1 + h_1^2 + 2h_0h_2 + 4h_1h_2 + 3h_2^2)},$$

$$d_2^{N-2} = \frac{4h_2(3h_0h_1 + 3h_1^2 + 2h_0h_2 + 4h_1h_2)}{(h_1 + h_2)(h_0 + h_1 + h_2)(h_0h_1 + h_1^2 + 2h_0h_2 + 4h_1h_2 + 3h_2^2)}.$$

#### A4 Case $k=0$

The first b-spline  $B_0(r)$  is constructed with two cubic polynomials defined on the interval between  $r_0$  and  $r_2$ :

$$B_0(r) = \sum_{j=0}^1 {}_0\rho_j(r), \quad (\text{A8})$$

$$r_j < r < r_{j+1}, \quad {}_0\rho_j(r) = 0 \quad \text{elsewhere}. \quad (\text{A9})$$

We use the same conditions as for the case  $k=1$  but have relaxed the condition that the first left-hand-side derivative vanish to avoid the trivial solution. The solution of the  $4 \times 4$  system yields

$$a_0^0 = \frac{4}{h_0(h_0 + h_1)(3h_0^2 + 3h_0h_1 + h_1^2)},$$

$$b_0^0 = 0,$$

$$c_0^0 = \frac{-12}{3h_0^2 + 3h_0h_1 + h_1^2},$$

$$d_0^0 = \frac{4(2h_0 + h_1)}{3h_0^2 + 3h_0h_1 + h_1^2},$$

$$a_1^0 = \frac{4}{h_1(h_0 + h_1)(3h_0^2 + 3h_0h_1 + h_1^2)},$$

$$b_1^0 = \frac{12}{(h_0 + h_1)(3h_0^2 + 3h_0h_1 + h_1^2)},$$

$$c_1^0 = \frac{-12h_1}{(h_0 + h_1)(3h_0^2 + 3h_0h_1 + h_1^2)},$$

$$d_1^0 = \frac{4h_1^2}{(h_0 + h_1)(3h_0^2 + 3h_0h_1 + h_1^2)}.$$

#### A5 Case $k=N-1$

The last b-spline,  $B_{N-1}(r)$ , is constructed with the two cubic polynomials on the interval between  $r_{N-3}$  and  $r_{N-1}$ :

$$B_{N-1}(r) = \sum_{j=0}^1 {}_{(N-1)}\rho_j(r), \quad (\text{A10})$$

$$r_{N+j-3} < r < r_{N+j-2}, \quad {}_{(N-1)}\rho_j(r) = 0 \quad \text{elsewhere}. \quad (\text{A11})$$

Intervverting right-hand side and left-hand side, we keep the same normalization and continuity conditions as for the case  $k=0$ . The solution of the  $4 \times 4$  system yields

$$a_0^{N-1} = \frac{4}{h_0(h_0 + h_1)(h_0^2 + 3h_0h_1 + h_1^2)},$$

$$b_0^{N-1} = c_0^{N-1} = d_0^{N-1} = 0,$$

$$a_1^{N-1} = \frac{-4}{h_1(h_0 + h_1)(h_0^2 + 3h_0h_1 + h_1^2)},$$

$$b_1^{N-1} = \frac{12}{(h_0 + h_1)(h_0^2 + 3h_0h_1 + h_1^2)},$$

$$c_1^{N-1} = \frac{12h_0}{(h_0 + h_1)(h_0^2 + 3h_0h_1 + h_1^2)},$$

$$d_1^{N-1} = \frac{4h_0^2}{(h_0 + h_1)(h_0^2 + 3h_0h_1 + h_1^2)}.$$